ISSN 0915-633X

NATIONAL INSTITUTE FOR FUSION SCIENCE

Ion and Electron Heating in ICRF Heating Experiments on LHD

K. Saito, R. Kumazawa, T. Mutoh, T. Seki, T. Watari, Y. Torē, D.A. Hartmann, Y. Zhao, A. Fukuyama, F. Shimpo, G. Nomura, M. Yokota, M. Sasao, M. Isobe, M. Osakabe, T. Ozaki, K. Narihara, Y. Nagayama, S. Inagaki, K. Itoh, S. Morita, A.V. Krasilnikov, K. Ohkubo, M. Sato, S. Kubo, T. Shimozuma, H. Idei, Y. Yoshimura, O. Kaneko, Y. Takeiri, Y. Oka, K. Tsumori, K. Ikeda, A. Komori, H. Yamada, H. Funaba, K.Y. Watanabe, S. Sakakibara, M. Shoji, R. Sakamoto, J. Miyazawa, K. Tanaka, B.J. Peterson, N. Ashikawa, S. Murakami, T. Minami, S. Ohakachi, S. Yamamoto, S. Kado, H. Sasao, H. Suzuki, K. Kawahata, P. deVries, M. Emoto, H. Nakanishi, T. Kobuchi, N. Inoue, N. Ohyabu, Y. Nakamura, S. Masuzaki, S. Muto, K. Sato, T. Morisaki, M. Yokoyama, T. Watanabe, M. Goto, I. Yamada, K. Ida T. Tokuzawa, , N. Noda, S. Yamaguchi, K. Akaishi, A. Sagara, K. Toi, K. Nishimura, K. Yamazaki, S. Sudo Y. Hamada, O. Motojima, M. Fujiwara

(Received - Jan. 25, 2001)

NIFS-683 Feb. 2001

RESEARCH REPORT
NIFS Series

TOKI, JAPAN

ION AND ELECTRON HEATING IN ICRF HEATING EXPERIMENTS ON LHD

K SAITO*, R KUMAZAWA, T. MUTOH, T SEKI, T WATARI, Y TORII*, D A HARTMANN**, Y. ZHAO***, A. FUKUYAMA****, F. SHIMPO, G. NOMURA, M. YOKOTA, M SASAO, M. ISOBE, M. OSAKABE, T OZAKI, K. NARIHARA, Y NAGAYAMA, S. INAGAKI, K. ITOH, S. MORITA, A.V. KRASILNIKOV*****, K OHKUBO, M. SATO, S. KUBO, T. SHIMOZUMA, H. IDEI, Y. YOSHIMURA, O. KANEKO, Y. TAKEIRI, Y. OKA, K. TSUMORI, K. IKEDA, A. KOMORI, H. YAMADA, H. FUNABA, K.Y. WATANABE, S SAKAKIBARA, M. SHOJI, R. SAKAMOTO, J. MIYAZAWA, K TANAKA, B J. PETERSON, N ASHIKAWA******, S MURAKAMI, T MINAMI, S. OHDACHI, S. YAMAMOTO*, S KADO, H. SASAO******, H SUZUKI, K. KAWAHATA, P deVRIES, M EMOTO, H. NAKANISHI, T. KOBUCHI******, N INOUE, N. OHYABU, Y NAKAMURA, S. MASUZAKI, S. MUTO, K. SATO, T. MORISAKI, M. YOKOYAMA, T. WATANABE, M GOTO, I. YAMADA, K. IDA, T. TOKUZAWA, N. NODA, S. YAMAGUCHI, K AKAISHI, A. SAGARA, K. TOI, K. NISHIMURA, K. YAMAZAKI, S. SUDO, Y HAMADA, O. MOTOJIMA, M. FUJIWARA

National Institute for Fusion Science, Toki, Japan. * Nagoya University, Faculty of Engineering, Nagoya, Japan.

** Max-Planck-Institute fuer Plasmaphysik, Garching, Germany.

*** Academia Sinica Plasma Physics Institute, Hefei, China.

**** Kyoto University, Department of Nuclear Engineering, Kyoto, Japan.

***** Troitsk Institute for Innovating and Fusion Research (TRINITI), Troitsk, Russia.

****** The Graduate University for Advanced Studies, Toki, Japan.

ABSTRACT. This paper reports on the Ion Cyclotron Range of Frequency (ICRF) heating conducted in 1999 in the 3rd experimental campaign on the Large Helical Device (LHD) with an emphasis on the optimization of the heating regime. Specifically, an exhaustive study of seven different heating regimes was carried out by changing the RF frequency relative to the magnetic field intensity, and the dependence of the heating efficiency on H-minority concentration was investigated. It was found in the experiment that both ion and electron heating are attainable with the same experimental setup by properly choosing the frequency relative to the magnetic field intensity. In the cases of both electron heating and ion heating, the power absorption efficiency depends on the minority ion concentration. An optimum minority concentration exists in the ion heating case while, in the electron heating case, the efficiency increases with concentration monotonically. A simple model calculation is introduced to provide a heuristic understanding of these experimental results.

Among the heating regimes examined in this experiment, one of the ion heating regimes was finally chosen as the optimized heating regime and various high performance discharges were realized with it.

Keywords: ICRF heating, ion heating, electron heating, heating efficiency, helical system, LHD

1. INTRODUCTION

Ion Cyclotron Range of Frequency (ICRF) heating is an established heating scheme in tokamaks. However, development of the ICRF heating in helical systems has not been so straightforward. The first ICRF heating was performed on the Model C stellarator by use of the slow wave [1]. It was followed by tokamak experiments and the regimes of fast wave heating were explored. Following these experiments, ICRF heating experiments were conducted in several helical devices; e.g. L-2 [2], Heliotron-E [3], ATF [4], CHS [5, 6], and W7-AS [7]. The performance of the ICRF heating has improved in recent experiments, particularly following the adoption of boronization. A variety of heating regimes is being explored examining their utility. In CHS, an electron heating regime by use of mode-converted IBW of low-field-side launch was found to be the best heating regime. In W7-AS, it has been shown that ICRF heating is possible using the following scenarios: D(H) minority heating, D,H mode conversion heating, and 2nd harmonic H heating. However, the stored energy attained remained less than 10 kJ in these experiments and more efforts are needed to establish ICRF heating in helical systems. Though ICRF heating experiments have been successfully performed in many tokamaks [8-10], early ICRF heating in helical systems often suffered from impurity problems. This may be attributed to the poor confinement of high energy ions as the orbits of trapped particles in helical devices do not nest nicely in the flux surfaces [11].

The LHD (Large Helical Device) is a l=2 and m=10 helical device with super-conducting coil windings. The major radius is 3.9 m and the minor radius is 0.6 m [12-15]. The major goal of experiments on the LHD is to establish its utility in nuclear fusion study by realizing high temperature (up to 10 keV) plasmas, high beta plasmas ($\langle\beta\rangle > 5\%$), and steady-state operation. The advantage of ICRF will be highlighted in the use for steady state operation, for ICRF has fewer technological problems than other heating methods.

Seven heating regimes specified by different combinations of magnetic field strength and frequency were investigated in the third campaign for the purpose of optimizing ICRF heating. This paper reports on the understanding of the mechanism of ICRF heating in the LHD. In section 2, the experimental setup is described. In section 3, the locations of the ion cyclotron resonance layer for seven values of the magnetic field and frequency are shown. In section 4-1, experimental results of the dependence of the heating mechanism on the magnetic field intensity and frequency are described. An account is given as to why the heating mechanism changes depending on the magnetic field intensity and frequency. In section 4-2, the dependence of heating efficiency on minority ion concentration is presented. In section 5, the existence of an optimum minority concentration in ion heating regimes is explained with a model. In section 6 the reason is discussed as to why an ion heating regime is regarded as the optimized heating regime. In section 7 conclusions are drawn.

2. EXPERIMENTAL EQUIPMENT

Figure 1 is a top view of the LHD, showing the location of heating devices: negative-ion-based neutral beam injection (NNBI), electron cyclotron heating (ECH), and ICRF heating. The main diagnostics used are an FIR interferometer, a bolometer, Thomson scattering, an electron cyclotron emission (ECE) system, a natural diamond detector (NDD), and Hα/HeI detectors.

There are various heating regimes in the ion cyclotron frequency range: ion-ion hybrid heating, minority ion heating, ion Bernstein wave (IBW) heating, and higher harmonic heating. RF frequency is dependent on the heating regime used as well as on magnetic field strength. Therefore, the ICRF system in the LHD is designed to cover a wide frequency range, from 25 MHz to 100 MHz. Two amplifier systems were used in the experiments, each of them consisting of a signal generator (SG), an intermediate power amplifier (IPA), a driver power amplifier (DPA), and a final power amplifier (FPA) The output power levels are 20 mW, 4 kW, 100 kW, and 2 MW, respectively. Tetrode tubes are used in the DPA and the FPA. In order to cover a wide frequency range, tunable double coaxial output cavities are employed in the DPA and the FPA. The amplifier was tested in a 1.6 MW/5,000 sec long pulse operation in the R&D phase [16]. The RF power is transmitted to the upper and lower loop antennas via a liquid impedance matching system [17-19].

Loading resistance changes depending on the frequency, the plasma density, and the distance between the loop antennas and the plasma. Therefore a tunable impedance matching system is necessary, and it must cover a wide frequency range. A liquid impedance matching system was employed to meet the needs of ICRF heating on the LHD: high power, steady state, and wide frequency range. This system consists of three liquid stub tuners. The liquid stub tuners utilize the difference of RF wavelength in gas and liquid due to the difference of the relative dielectric constants. The surface level of the liquid is changed for impedance matching while sliding contactors are used in conventional stub tuners. The liquid stub tuners were verified to be a reliable RF component in R&D work; it withstood 63 kV for 10 seconds and 50 kV for 30 minutes.

A pair of loop antennas [20, 21] were used in the experiment; they have RF current perpendicular to the magnetic field in order to launch the fast wave. The RF power is fed from upper and lower ports of the LHD through ceramic feed-throughs [22]. The plasma cross-section in front of the loop antennas is vertically elongated. The dimensions of the loop antennas are 46 cm in total width (30 cm in strap width), 120 cm in length (including upper and lower antennas), and 17 cm in depth. The loop antennas are twisted to fit the last closed flux surface (LCFS) of the helical plasma and are movable by 16 cm in the radial direction to adjust the distance between the antennas and LCFS. The straps, back plates, Faraday shields, and side protectors are water-cooled and can withstand over 30 minutes in steady-state test operation.

3. LOCATIONS OF ION CYCLOTRON RESONANCE LAYERS

Plasma is heated in ion-ion-hybrid and minority-ion heating regimes, with helium the majority species and hydrogen the minority species. The experiment was conducted under various conditions with different magnetic field strengths (<2.893T) and RF frequencies (38.47MHz, and 28.4MHz). Seven different combinations of magnetic field strength and RF frequency are shown in Table 1, where B_0 and f are the magnetic field strength on the magnetic axis and the RF frequency, respectively. The ratio of the frequency to the ion cyclotron frequency of hydrogen on the magnetic axis, ω/ω_{ci}, is the key parameter, and determines the location of the cyclotron layer. It should be noted that Heliotron/Torsatron type helical systems have a saddle-shaped non-uniformity of the magnetic field strength across the minor cross section of the plasma. The saddle point is on the equatorial plane between the plasma axis and the antennas. The change of the magnetic field intensity on the axis provides various interesting heating regimes.

Figure 2-(a) shows the locations of the minority ion cyclotron resonance layer for seven cases from Type-1 to Type-7. In the case of Type-1 the cyclotron resonance layer of the minority ion splits into an upper and lower pair located near the periphery. The magnetic field strength decreases toward them. In the case of Type-5 the minority ion cyclotron resonance layer is located near the saddle point. In Type-6 the minority ion cyclotron resonance layer just crosses the magnetic axis.

Figure 2-(b) shows the layers of ion cyclotron resonance, ion-ion hybrid resonance, R-cutoff, and L-cutoff for the typical case of a Type-5 regime as an example. Here, dielectric constants of the cold-plasma approximation were used. A density profile of the form $n_e = n_{e0}(1-\rho^8)$ is assumed in the calculation of Fig.2-(b), where ρ is the normalized minor radius and $n_{e0} = 1.0\times10^{19}$ m^{-3} is the electron density on the magnetic axis. The minority ion ratio, $n_H/(n_H + n_{He}) = 5\%$, and the wave number parallel to the magnetic field line, $k_z = 5$ m^{-1}, are used in this calculation.

4. EXPERIMENTAL RESULTS

ICRF heating was first examined back in 1998 on the LHD in the 2nd experimental campaign. It was carried out using helium plasma with minority hydrogen ions. The magnetic field strength on the magnetic axis was B_0=1.5 T and the applied frequency was f=25.6 MHz. The position of the magnetic axis was R_0=3.75 m, which is taken as the standard configuration. A pair of loop antennas having current straps 30 cm in width and 60 cm in length was used in this experiment. ICRF power of 300 kW was applied to the ECH target plasma and the increase of plasma stored energy was 13 kJ [23]. Though evidence of plasma heating was obtained, the quality of the heating was not high enough to assure the applicability of ICRF Heating. The parameter, ω/ω_{ci}, of the heating regime used in the second campaign is higher than that of the Type-7 regime in Table 1.

The same ICRF system was used in the 3rd campaign. However, there was the following change in the

experimental conditions: The available magnetic field strength was increased from 1.5T up to 2.9T. Two RF frequencies, 38.47MHz and 28.4MHz, were used in the experiment depending on the heating regime. The former frequency is higher than that used in the second campaign. The position of the magnetic axis was shifted from the standard 3.75 m to 3.6 m in order to improve the confinement of trapped ions. The increase of the loading resistance due to the use of a higher frequency (38.47MHz) is regarded as one of the key factors facilitating injection of higher power.

4.1 Dependence of the heating mechanism on the location of the cyclotron resonance layer

In this section, the fraction of ICRF power directly absorbed by electrons is measured for seven heating regimes in order to address the heating mechanisms of the respective heating regimes. In order to provide an idea of the quality of the heating depending on the parameter range, time histories of two typical shots are shown in Figures 3-(a) and (b). The discharge shown in Fig. 3-(a) represents the Type-1 heating regime. The plasma stored energy was $W_p = 36$ kJ and the line averaged electron density was $\overline{n_e} = 0.76\times10^{19}$ m^{-3} with the injected ICRF heating power $P_{ICH} = 235$ kW at t=2.0 sec. Electron heating was dominant in this discharge, as will be described later. The discharge shown in Fig. 3-(b) represents the case of Type-5. The plasma stored energy, the line-averaged electron density, the electron temperature on the magnetic axis, and the ICRF heating power at the time of t=5.11sec were $W_p = 177$ kJ, $\overline{n_e} = 1.2\times10^{19}$ m^{-3}, $T_{e0} = 2.1$ keV, and $P_{ICH} = 1.3$ MW, respectively. Ion heating was dominant in this discharge. Time histories of the shots for other heating regimes are abbreviated for they have similar features to the two cases. The electron density was measured by a 13 channel FIR interferometer, the electron temperature was measured by a Thomson scattering measurement (106 channels with sampling time of 20 msec), and the radiation power was measured by a wide angle bolometer [24].

Figure 3-(c) is also taken from the case of Type-5. Here, ICRF heating is applied to the NBI target plasma with parameters $\overline{n_e} = 2.0\times10^{19}$ m^{-3} and T_{e0}=1.9 keV. Then the absorbed NBI power, P_{NBI} was 1.3MW. The plasma stored energy increased from 230 kJ to 340 kJ and T_{e0} reached 2.5 keV with $P_{ICH} = 1.3$ MW. This shot suggests that ICRF heating can be applied in high power heating experiments in combination with NBI.

Figure 4 shows the ion energy distribution in the discharge of Fig. 3-(c) observed by a natural diamond detector (NDD) [25, 26], which detects the high-energy neutrals escaping out of the plasma via a charge exchange process. The line of sight is perpendicular to the plasma column so that the population of ions with the perpendicular pitch angle is measured. The ordinate is the direct count number of neutral particles for 0.1 sec. In this figure, the labels A to D with arrows indicate the time of measurement shown in Fig. 3-(c) by arrows. The range below 30 keV is affected by the thermal noise of the preamplifier. In this discharge, the high-energy ion tail was observed after ICRF heating was turned on (B) while there was no observable high-energy ion tail in the NBI-only phase (A). Note that NBI is of tangential injection. The high energy tail is sustained up to the end of the RF pulse (C and D). Figure 4, therefore, indicates that ions are heated directly by the excited fast wave in the case of Type-5.

The fraction of the power absorbed by electrons is calculated from the decay of electron temperature as the RF is turned off. Figures 5-(a) and (b) show the temporal behavior of the electron temperature measured by ECE of the 2nd harmonic extraordinary wave in the shots of Fig. 3-(a) and (b), respectively. The sampling time of ECE is 0.1 msec. It was found in Figs. 5-(a) that the electron temperature decays immediately after ICRF heating is turned off, which indicates that there is direct heating of electrons in the case of Type-1. On the contrary, in the Type-5 regime, the temperature shows small change as the RF is turned off as shown in Fig. 5-(b). Therefore direct electron heating is found to be very weak in the Type-5 regime. Since there is an increase in stored energy, it is deduced that the power was absorbed mainly by ions.

To estimate the fraction of the direct power absorption by electrons, the electron power balance equation was used:

$$\frac{3}{2}\frac{\partial}{\partial t}(n_e T_e) = \frac{1}{r}\frac{\partial}{\partial r}(r n_e \chi_e \frac{\partial T_e}{\partial r} + \frac{3}{2} r D T_e \frac{\partial n_e}{\partial r}) + P_{ei} - P_{rad} + P_e \qquad (1)$$

χ_e and D are the thermal and particle diffusivity of electrons, respectively. P_{ei}, P_{rad}, and P_e are power to electrons from ions (including those from majority and from ICRF enhanced minority ion tail), the radiation loss, and the power absorbed by electrons, respectively. Assuming that the quantities on the right hand side are continuous except for P_e between before and after turning off the RF power, the following equation is obtained:

$$P_e = \frac{3}{2} n_e \{(\mathrm{d}T_e/\mathrm{d}t)_{t=t_0-0} - (\mathrm{d}T_e/\mathrm{d}t)_{t=t_0+0}\} \qquad (2)$$

This method was applied to the Type-1 regime giving the radial profile of the absorbed power by electrons as shown in Fig. 6-(a). The power was estimated from the decay of the electron temperature. Since the time span was taken to be shorter (a few milliseconds) than the energy relaxation time between the minority ion tail and electrons, the power estimated in this paper is regarded to be that absorbed by electrons directly. (ex. the relaxation time is about 30msec in the case of Fig. 5 (a) at ρ=0.73). Thus the possibility of power flow from ions is ruled out. The integrated power inside a magnetic flux surface $\int_0^{\rho} P_e(\mathrm{d}V/\mathrm{d}\rho)\,\mathrm{d}\rho$ is shown in Fig. 6-(b) by a solid line, where $V = V(\rho)$ is the plasma volume surrounded by the flux surface. It gives 170 kW for the total absorbed power by electrons, $P_{electron}$, in the case of the Type-1 regime. On the other hand, the total absorbed power by the plasma, P_{abs}, is deduced from the change of the slope of plasma stored energy measured with the diamagnetic loop after the turn-off of RF power. It was found that the total absorbed power, P_{abs} was 173 kW. The agreement of the power absorbed by electrons with the total power means that the power is absorbed mostly by electrons. By applying the same procedure, the fractions of electron heating, $P_{electron}/P_{abs}$ were obtained for the other types of heating regimes. The results are shown by solid circles in Fig. 7 with the abscissa showing the ratio of frequency to the ion cyclotron frequency of hydrogen on the magnetic axis, ω/ω_{ci}, appearing in Table 1. The parameter range covered by the shots used in Fig. 7 is shown in Table 2. In the case of

Type-1, the power was absorbed mainly by electrons while, in the cases of Type-4 to Type-6, the power was mainly absorbed by ions. The cases of Type-2 and 3 fall in between, and both electron heating and ion heating occur In general, the diamagnetic measurement gives perpendicular pressure and total pressure is obtained assuming isotropy of the distribution which may not be valid in high power experiments. However, this effect is estimated to be small in this experiment, where power density is low

The RF power is supposed to be absorbed by electrons through the ion Bernstein wave (IBW), to which fast wave is mode-converted at the ion-ion hybrid resonance layer. We estimate the fraction of the power absorbed by electrons by estimating the power mode-converted to IBW. Further, it is assumed that the mode-conversion coefficient is unity for the high-magnetic-field-side launch and zero for the low-magnetic-field-side launch, since the mode-conversion ratio for high-field-side injection is much larger than that for low-field-side injection. We define L_e and L_i as shown in Fig. 8 and evaluated the RF power fraction from the high magnetic field side as $L_e/(L_e+L_i)$. The value of $L_e/(L_e+L_i)$ depends most strongly on ω/ω_{ci} and weakly on other parameters, for which $n_{e0}=1\times10^{19}\mathrm{m}^{-3}$, $n_H/(n_H+n_{He})=30\%$, and $k_z=5\mathrm{m}^{-1}$ are assumed. In Fig. 7, the calculated $L_e/(L_e+L_i)$ is shown by a dashed line compared with the experimentally obtained fraction of the power absorbed by electrons, $P_{electron}/P_{abs}$. It is worthwhile to mention that the simple paradigm that electrons are heated for high-field-side launch can explain the ICRF heating mechanism in a helical system.

So far, the electron power deposition profile has been discussed based on the temporal behavior of the electron temperature just after the RF power is turned off. Insight into the deposition profile is obtained also from the temperature profile obtained from the Thomson scattering measurement. Figure 9 shows the electron temperature profile in the case of Type-2. It has a very flat temperature profile, suggesting that power deposition in the plasma core region is small. The peak of the deposition is identified to be $\rho=0.7$ because the electron temperature profile has the largest curvature there. For the same discharge, the fraction of electron heating, $P_{electron}/P_{abs}$ was deduced to be 50% from an analysis based on ECE measurements, and the peak of the power deposition was at $\rho=0.60$. The peak of the deposition profile obtained from Thomson scattering measurement, with the assumption of T_e=T_i, is considered to be that of total power. It is expected from theory that electrons are heated at the ion-ion hybrid resonance layer ($\rho=0.60$) and ions are heated at the cyclotron resonance layer of hydrogen ($\rho=0.80$). Therefore, the peak of the power deposition is expected to be around $\rho=0.6\sim0.8$, which agrees with the value 0.7 obtained from the Thomson data.

4.2 Dependence of heating efficiency on minority ion concentration

H-concentration plays an important role in ICRF heating. In this study the ratio of Hα/HeI was measured and used as an indicator. For this purpose, several monitors to measure the intensity of Hα (656.3 nm) and HeI (587.6 nm) were installed on the vacuum ports adjacent to the ICRF antennas. In many tokamak ICRF experiments where hydrogen and deuterium is used, the Hα/Dα ratio is

conventionally used as an indicator of hydrogen concentration. In this experiment, where He is used in place of D, the ratio of Hα/HeI is measured. The relation between Hα/HeI and $n_H/(n_H+n_{He})$ may not be simple. However, since the Hα/HeI ratio has a strong correlation with the heating efficiency and the results were reproducible, it was used in practice as a good indicator of $n_H/(n_H+n_{He})$ throughout the ICRF experiment in the third campaign. In this section, the relation between the heating efficiency and the ratio Hα/HeI is studied for two cases of electron heating and ion heating.

4.2.1 Electron heating regimes

Figures 10-(a) and (b) compare two discharges of Type-1, where pure electron heating dominates as shown in Fig. 7. The ICRF heating power was 200 kW for both cases with a similar value of the line averaged electron density, $\overline{n_e}$=0.6~0.8×10^{19} m^{-3}. When the ratio Hα/HeI is small (less than 4), the plasma stored energy decreases gradually in time as shown in Fig. 10-(a) and the heating efficiency is 30%, as it is deduced from the ratio of the absorbed power, P_{abs}, to the injected RF power from the antennas, P_{ICH}. On the other hand when the ratio Hα/HeI is large (~ 6), the plasma stored energy increases in time as shown in Fig. 10-(b) although the injected ICRF heating power is almost the same. Figure 11 shows the relation between the heating efficiency and the ratio Hα/HeI. Data are taken from ICRF shots with a similar value of the line-averaged electron density ($0.5<\overline{n_e}<1.0\times10^{19}$ m^{-3}). In the case of Type-1, where electron heating dominates, the basic tendency is that the heating efficiency increases with increasing Hα/HeI ratio.

Figures 12-(a) and (b) show the calculated layers of ion cyclotron resonance, ion-ion hybrid resonance, R-cutoff, and L-cutoff in the case of Type-1. Figure 12-(a) is for the case of $n_H/(n_H+n_{He})=10\%$, representing the low minority concentration, and figure 12-(b) is for the case of $n_H/(n_H+n_{He})=50\%$, representing the high minority concentration. In both cases k_z is assumed to be 5 m^{-1}. In the case of $n_H/(n_H+n_{He})=10\%$, the ion-ion hybrid resonance and L-cutoff layers cannot be distinguished from each other, as shown in Fig. 12-(a). In the case of $n_H/(n_H+n_{He})=50\%$, however, the evanescent region between the ion-ion hybrid resonance layer and the L-cutoff layer is wide as shown in Fig. 12-(b). The mode-conversion ratio is larger with a wider evanescent region causing stronger wave absorption in the case of high-magnetic-field-side injection. This may be the reason for the high absorption efficiency obtained with a large Hα/HeI ratio in Type-1 regime. The resonance layer shifted toward the core region of the plasma as the H-concentration increased and this may also have contributed to the improvement of efficiency.

So far, Hα/HeI has been used as a measure of $n_H/(n_H+n_{He})$. Here, we try to calibrate them to deduce the absolute value of $n_H/(n_H+n_{He})$ by comparison of the experimental observations of the power deposition profile with theoretical calculations. It is assumed that electron heating is strongest at the magnetic flux surface where the ion-ion-hybrid layer is tangent because the ion-ion hybrid resonance layer occupies the largest area. In discharge #13413, shown in Fig. 3-(a), the radius of tangency is determined to be $\rho=0.74\pm0.05$ in the case of $n_H/(n_H+n_{He})=40\%$, where the electron density profile

measured by FIR interferometer was used. The uncertainty of ± 0.05 is due to the allowed range of k_z ($0<k_z<6.9$ m^{-1}). For the waves with $k_z > 6.9$ m^{-1}, the ion-ion hybrid resonance layer shifts to outside of the R-cutoff layer and they may not contribute to electron heating. Similarly, the radii of tangency are determined for $n_H/(n_H + n_{He}) = 30\%$ and 50% to be $\rho = 0.80 \pm 0.04$ and $\rho = 0.66 \pm 0.07$, respectively. On the other hand, the peak of the power absorption is determined from Figs. 6-(a) and (b) to be $\rho = 0.73$, which is approximately the radius of tangency of the hybrid layer for 40%. The ratio Hα/HeI =5.3 in the same shot is thus associated with the minority ion ratio $n_H/(n_H + n_{He})$ of 40%. This calibration is done for the Type-1 regime only and can be extended to other regimes by assuming the same coefficient of proportionality

4.2.2 Ion heating regimes

Figures 13-(a), (b), and (c) show the dependence of the heating efficiency on the ratio of Hα/HeI in the case of Type-4, Type-5, and Type-6, respectively. They are in the ion heating regimes as is readily seen from Fig. 7. Data points are grouped with respect to line averaged electron density as distinguished by different symbols. In the case of Type-4 (Fig. 13-(a)), the heating efficiency increases as the ratio Hα/HeI decreases within the range where data points exist reaching 80% with the lowest value of Hα/HeI=0.8. In the case of Type-5 there is a maximum in the heating efficiency (80%) around Hα/HeI=1. In the case of Type-6 the cyclotron resonance layer crosses the magnetic axis as shown in Fig. 2-(b). Therefore, this regime was considered to be one of the best heating regimes. However, as shown in Fig. 13-(c), it was found that the heating efficiency is not as good as those of Type-4 and 5. The interpretation of the experimental results is given in the next section.

Thus the Type-5 regime was taken as the optimum heating regime and many experiments were conducted with its optimum Hα/HeI ratio. The success of the high power ICRF heating experiments in the third campaign is summarized as follows: 1) A plasma with stored energy of 200 kJ ($\bar{n}_e = 1.8\times10^{19}$ m^{-3}, T_{e0}=1.7 keV) was sustained for 5 seconds with ICRF heating power alone (P_{ICH}=1.2 MW). 2) There was no sign of accumulation of impurities and an even longer plasma duration exceeding 1 minute was obtained with reduced power P_{ICH}=0.7 MW. The parameters of this shot $\bar{n}_e = 1.0\times10^{19}$ m^{-3} and T_{e0}=2 keV were maintained throughout this long pulse shot [27, 28]. 3) ICRF heating power of P_{ICH}=1.3 MW was applied to the NBI heated target plasma. The plasma stored energy was increased from 230 kJ to 340 kJ attaining parameters of $\bar{n}_e = 2.0\times10^{19}$ m^{-3} and T_{e0}=2.5 keV.

5. A MODEL CALCULATION OF ION HEATING EFFICIENCY

In sections 3 and 4, the dependence of the heating efficiency on the magnetic field intensity and the minority ion ratio was discussed These experimental results contain information which is necessary in order to understand the wave physics which underlies the experiment. Particularly, it is interesting to

attempt to account for the fact that the best heating was obtained in Type-5 regimes. Since it is known that the existence of reasonably strong wave absorption is one of the necessary conditions of good wave heating, we try to compare the heating regimes of ion heating, Types 4-6, in view of the wave absorption intensity.

It is known in the case of ion heating that the power absorption depends on the left hand component of the RF electric field [29]:

$$P=\frac{\varepsilon_0}{2}\Pi_j^{\,2}\frac{\pi^{1/2}}{|k_z|(2T_j/m_j)^{1/2}}\exp\left\{-\left(\frac{\omega-\Omega_j}{k_z(2T_j/m_j)^{1/2}}\right)^2\right\}|E_{\mathrm{Left}}|^2 \tag{3}$$

where j is a label of the resonant particle. Π_j and Ω_j are respectively the plasma and cyclotron frequencies of the j-th species. We simply assume that the RF electric field strength is constant, $|E_0|$ in the region where the fast wave can propagate, and zero in the other region to explain the minority ion ratio dependence of the heating efficiency. We relate the left hand component $|E_{\mathrm{Left}}|^2$ to the absolute value of $|E_0|^2$ by the following equation:

$$|E_{\mathrm{Left}}|^2=\frac{|E_x+iE_y|^2}{|E_x+iE_y|^2+|E_x-iE_y|^2}|E_0|^2=\left(\frac{1}{2}+\frac{\mathrm{Im}(A)}{|A|^2+1}\right)|E_0|^2 \tag{4}$$

where,

$$A=\frac{E_x}{E_y}=\frac{K_{xy}}{n_z^{\,2}-K_{xx}} \tag{5}$$

Substitution of equations (4) and (5) into equation (3) yields the power per unit volume:

$$\frac{P}{|E_0|^2}=\frac{\varepsilon_0}{2}\Pi_j^{\,2}\frac{\pi^{1/2}}{|k_z|(2T_j/m_j)^{1/2}}\exp\left\{-\left(\frac{\omega-\Omega_j}{k_z(2T_j/m_j)^{1/2}}\right)^2\right\}\left\{\frac{1}{2}+\frac{\mathrm{Im}(K_{xy}/(n_z^{\,2}-K_{xx}))}{|K_{xy}/(n_z^{\,2}-K_{xx})|^2+1}\right\} \tag{6}$$

Therefore, the intensity of the wave absorption is calculated by using the local plasma parameters.

Shown in Figs. 14-(a), (b), and (c) are the cyclotron layers and the calculated power absorption regions for Type-4, Type-5, and Type-6 regimes, respectively. Here, the power absorption region is defined by a region where absorbed power is larger than 1 kW/m^3 for an RF field of 1 kV/m as calculated by use of equation (6). In these calculations, the minority ion ratio is $n_{\mathrm{H}}/(n_{\mathrm{H}}+n_{\mathrm{He}})=5\%$, and the wave number parallel to the magnetic field line is $k_z=5\ \mathrm{m}^{-1}$, the electron density on the magnetic axis is $n_{e0}=1\times10^{19}\ \mathrm{m}^{-3}$, the temperature on the magnetic axis is T_{e0}=$T_{\mathrm{H}0}$=$T_{\mathrm{He}0}$=2 keV and the profiles of electron density and temperature are given as $n_e=n_{e0}(1-\rho^8)$ and $T_e=T_{\mathrm{H}}=T_{\mathrm{He}}=T_{e0}(1-\rho^2)$, respectively. It was found that in the case of Type-5 the heating region is quite large compared with that of other types. This is due to a small gradient of the magnetic field strength near the saddle point. Figure 15 shows the

calculated power deposition profiles, which are obtained by integrating $P/|E_0|^2$ on the magnetic flux surface. The same RF electric field strength was used for the calculations for the three cases

The injected ICRF heating power, P_{ICH} is the sum of P_{abs} and P_{loss}. Here, P_{abs} is the part which contributes to plasma heating and P_{loss} is the total power loss including the dissipation on the vacuum vessel wall and the power used to disturb the peripheral plasma. P_{abs} and P_{loss} may be written in a quadratic form in electric field strength :

$$P_{abs} = \alpha|E_0|^2 \qquad \text{and} \qquad P_{loss} = \beta|E_0|^2$$

The heating efficiency, η is then defined as the ratio of the absorbed power, P_{abs}, to the injected ICRF heating power, P_{ICH}, as:

$$\eta = \frac{P_{abs}}{P_{ICH}} = \frac{\alpha|E_0|^2}{\alpha|E_0|^2 + \beta|E_0|^2} = 1 - \frac{\beta}{\alpha+\beta}$$

The value α is obtained by integrating equation (6) over the entire plasma volume and the k_z spectrum of the wave The plasma is assumed to be two-dimensional having the same cross-section along the toroidal direction. In the heuristic consideration below, β is held constant since the RF frequency is fixed. Figure 16 shows the relation between the calculated heating efficiency and the minority ion ratio. Here, the value of β was selected so that the calculated η agrees with the experimental result that the maximum heating efficiency of Type-5 regime is about 80%. The efficiency decreases with a lower H-concentration due to the lack of resonant particles (H) and decreases with a higher H-concentration due to the reduction of $|E_{Left}|$ near the cyclotron resonance layer.

As shown in Fig. 16, it was found that the heating efficiency was best in the case where the layer of the minority ion cyclotron resonance is located near the saddle point. This is because the heating region is large as shown in Fig. 14-(b). The theoretical optimum H-concentration for a Type-5 regime is found to be 2~6% in Fig.16. The highest efficiency is obtained in the experiment for Type-5 with Hα/HeI ratio around 1 as seen in Fig.13. This translates into an optimum minority ion ratio $n_H/(n_H + n_{He})$ of 10% by applying the calibration factor obtained in section 4-2-1 to the Type-5 regime. Though the optimum H-concentrations differ between the experiment and theoretical prediction, the dependence of the heating efficiency on the minority ion ratio agrees qualitatively.

As for the Type-4 regime, experimental data are available only within the parameter range 0.8<Hα/HeI<10 which is translated into 9%< $n_H/(n_H + n_{He})$ <56%. Figure 16 also succeeds in explaining the experimental result that efficiency is improved with decreasing H-concentration within the experimental parameter range.

The power absorption is small in the case of Type-6, as shown in Fig.13-(c), and it does not have a clear dependence on the H-concentration. However, the theory agrees with the experiment in the prediction that the absorption mechanism is weak.

6. DISCUSSION

In the ICRF experiments in the 3rd campaign, the Type-5 regime was found to be the best heating regime. The excellence of the regime is easily seen in table 2, where achieved stored energy, operational plasma density, and electron temperatures are higher than those of other heating regimes. However, it is worthwhile to note that the frequency is lower for three regimes of electron heating from Type-1 to Type-3. The difference in the attained parameters between the electron heating and ion heating mostly comes from the difference of the injected power and the attainable plasma density, which is due to the difference of the applied frequency. The electron heating regimes have similarly high quality as far as the impurity problem is concerned. In more detail, electron heating regimes have more off-axis power deposition profiles than that of the Type-5 regime and, in this sense, the former may be inferior to the latter, reducing the energy confinement slightly. Therefore, as the Type-5 regime is taken as the best heating regime, the engineering merit of power handling is in itself not insignificant, and is included in the evaluation.

7. CONCLUSION

ICRF heating experiments were successfully conducted in the LHD, realizing power injection exceeding 1 MW and long pulse operation reaching 1 min with reduced power of 0.7 MW. The best results were obtained with B_0=2.75 T and f=38.47 MHz, where the minority ion cyclotron resonance layer is located near the saddle point. In this optimized heating regime, the RF power was almost completely absorbed by ions. Therefore, these experimental results signify that ion heating is as viable a method in helical devices as it is in tokamaks. These results were obtained in a systematic scan of magnetic field and RF frequency. For us another heating regime of interest was the one where the cyclotron resonance layer of minority ions crosses the magnetic axis. However, the heating efficiency of this heating regime was not as high as that of the optimized heating regime. That the best heating results occur in the optimized regime can be attributed to the fact that a large absorption area is available near the saddle point where the gradient of magnetic field strength is small.

On the other hand electron heating occurs with B_0=2.75 T and f=28.4 MHz, where the minority ion cyclotron resonance layer splits into an upper and lower pair located near the periphery. Due to the unique distribution of the magnetic field of a helical system, some fraction of the ICRF power is incident from the high-field side and the remaining fraction from the low-field side. The change of the heating mechanism from ion heating to electron heating is attributed to the change of this fraction, which depends on the central magnetic field intensity and the RF frequency.

The dependence of the heating efficiency on the minority concentration was also investigated in order to optimize ICRF heating. It was found that an optimum minority concentration exists in the ion heating regime. A model calculation was made to explain the observed dependence of the heating efficiency on

the minority concentration. It was shown that the optimum concentration arises because heating efficiency falls due to the lack of minority ions which absorb wave energy with lower H-concentration, and due to the reduction of the left hand component of the electric field with higher H-concentration.

In the electron heating regime it was found that the efficiency increases with increasing H-concentration. This dependence is associated with the fact that the distance of the ion-ion hybrid resonance layer from the L-cutoff layer is greater, with a larger value of the H-concentration giving a larger mode-conversion ratio. The ion-ion hybrid resonance layer shifts to the central region as the H-concentration is increased. This may also contribute to the improvement of performance at high concentrations.

Acknowledgements

The authors wish to thank the technical staff of the LHD group in the National Institute for Fusion Science for their helpful support during this work.

References

[1] YOSHIKAWA, S., ROTHMAN, M.A., SINCLAIR, R.M., Phys. Rev. Lett. **14** (1965) 214.

[2] BAYUK, V.A., et al., European Physical Society, pt.1 373-376. (proc. 11th European Conference on Controlled Fusion and Plasma Physics, 1983)

[3] MUTOH, T., et al., Nucl. Fusion **24** (1984) 1003.

[4] KWON, M., et al., Nucl. Fusion **32** (1992) 1225.

[5] NISHIMURA, K., et al., Fusion Engineering and Design **26** (1995) 179.

[6] MASUDA, S., et al., Nucl. Fusion **37** (1997) 53.

[7] HARTMANN, D.A., et al., Fusion Energy 1998, vol.2, p575, C&S Papers Series 1/p (1999).

[8] KIMURA, H., et al., Nucl. Fusion **19** (1979) 1499.

[9] FUJII, T., et al., Fusion Engineering and Design **26** (1995) 377.

[10] ROGERS, J.H., et al., Fusion Energy 1996, vol.3, p317 (1997).

[11] WATARI, T., Plasma Physics and Controlled Fusion **40** (1998)13.

[12] MOTOJIMA, O., et al., Fusion Engineering and Design **20** (1993) 3.

[13] IIYOSHI, A., YAMAZAKI, K., Physics of Plasmas **2** (1995) 2349.

[14] FUJIWARA, M., et al., Journal of Fusion Energy **15** (1996) 7.

[15] MOTOJIMA, O., et. al., IAEA-CN-69/ FT1/2 (1998).

[16] KUMAZAWA, R., et al., Proc. of 19th Symp. on Fusion Tecnology **1** (1996) 617.

[17] KUMAZAWA, R., et al., Review of Scientific Instruments **70** (1999) 2665.

[18] KUMAZAWA, R., et al., Radio Frequency Power in Plasmas,
13th Topical Conference, p441 (1999)
[19] SAITO, K., et al., submitted to Review of Scientific Instruments.
[20] MUTOH, T., et al., Proc. of 14th Symp. on Fusion Engineering **1** (1992) 103.
[21] MUTOH, T., et al., Proc. of 16th Symp. on Fusion Engineering **2** (1995) 1078.
[22] MUTOH, T., et al., Fusion Technology **35** (1999) 297.
[23] MUTOH, T., et al., Plasma Physics and Controlled Fusion **42** (2000) 265.
[24] PETERSON, B.J., et al.,
Proc. of 26th EPS Conf. on Contr. Fusion and Plasma Physics **23** (1999) 1337
[25] KRASILNIKOV, A.V., et al., Nucl.Fusion **39** (1999) 1111.
[26] ISOBE, M., et al., to be published in Review of Scientific Instruments.
[27] KUMAZAWA, R., et al., Journal of Plasma and Fusion Research SERIES Vol.3, 352 (2000).
[28] WATARI, T., et. al., IAEA-CN-77/ EX8/4 (2000).
[29] STIX, T.H., THE THEORY OF PLASMA WAVES, McGraw-Hill, (1962), p.207.

Figure Captions

Fig. 1 Top view of the LHD with heating devices and diagnostics.

Fig. 2 (a) Ion cyclotron resonance layers of hydrogen in the cases of Type-1 to Type-7. (b) Location of layers of ion cyclotron resonance, ion-ion hybrid resonance, R-cutoff, and L-cutoff in front of ICRF antennas in the case of Type-5. In this calculation $n_{e0} = 1.0 \times 10^{19}\ \mathrm{m}^{-3}$, $n_H/(n_H + n_{He}) = 5\%$, and $k_z = 5\ \mathrm{m}^{-1}$ were used.

Fig. 3 (a) A discharge of Type-1 regime, i.e. in the case that the cyclotron resonance layer of the minority ion splits into an upper and lower pair locating near the periphery. (b) A discharge of the Type-5 regime, i.e. in the case that the minority ion cyclotron resonance layer is located near the saddle point. (c) An additional ICRF heating of the NBI target plasma in the case of Type-5.

Fig. 4 The energy distribution of neutral particles detected by a natural diamond detector (NDD) in the discharge of Fig. 3-(c). The labels A to D denote the times of measurement as shown in Fig. 3-(c) by arrows. An energetic tail extending to 100 keV is observed after ICRF heating turn-on (B) while no high energy ion tail is observed in the NBI only phase (A).

Fig. 5 Electron temperature measured by ECE: (a); in the discharge of Type-1. (b); in the discharge of Type-5.

Fig. 6 (a) Absorbed power by electrons per unit volume in the discharge of Type-1. (b) $\int_0^{\rho} P_e(\mathrm{d}V/\mathrm{d}\rho)\,\mathrm{d}\rho$ (solid line) is the integration of the absorbed power inside a flux surface labeled ρ. $P_e \mathrm{d}V/\mathrm{d}\rho$ versus ρ is also shown by a dashed line.

Fig. 7 Fraction of electron heating, $P_{electron}/P_{abs}$, for the seven types of regimes given in Table-1. The abscissa is the ratio of RF frequency to the ion cyclotron frequency of hydrogen on the magnetic axis, which depends on the location of the ion cyclotron resonance layer of hydrogen. The dashed line is the fraction of high magnetic field side injection as estimated by $L_e/(L_e + L_i)$ with L_e and L_i defined in Fig. 8.

Fig. 8 The definition of L_e and L_i. L_e and L_i measure high field and low field side excitation of the wave. They are associated with the fractions of power absorbed by electrons and ions, respectively.

Fig. 9 An electron temperature profile measured by Thomson scattering in the case of Type-2. In this discharge, the power was dominantly absorbed around $\rho = 0.7$.

Fig. 10 Discharges of Type-1: (a); small Hα/HeI ratio. (b); large Hα/HeI ratio. There is a difference in plasma stored energy between the two shots.

Fig. 11 Dependence of the heating efficiency on Hα/HeI in the discharge of Type-1.

Fig. 12 Calculated positions of layers of ion cyclotron resonance, ion-ion hybrid resonance, R-cutoff, and L-cutoff in the case of Type-1: (a); $n_H/(n_H+n_{He})=10\%$. (b); $n_H/(n_H+n_{He})=50\%$.

Fig. 13 The dependence of heating efficiency on Hα/HeI in the cases of (a) Type-4, (b) Type-5, and (c) Type-6.

Fig. 14 Calculated power absorption zones in the cases of (a) Type-4, (b) Type-5, and (c) Type-6.

Fig. 15 Calculated power deposition profiles with the same RF electric field strength in the cases of Type-4 (dashed line), Type-5 (solid line), and Type-6 (dot-dash-line).

Fig. 16 Calculated heating efficiency versus H-concentration in the cases of Type-4 (dashed line), Type-5 (solid line), and Type-6 (dot-dash-line).

Table 1. Magnetic Field Strengths and RF Frequencies.

type	B_0 (T)	f (MHz)	ω/ω_{c_i}
1	2.75	28.4	0.677
2	2.5	28.4	0.745
3	2.3	28.4	0.810
4	2 893	38.47	0.872
5	2.75	38.47	0.918
6	2.5	38.47	1.009
7	2.3	38.47	1.097

B_0 : magnetic field strength on axis (T).

f : RF frequency (MHz).

ω / ω_{c_i} : ratio of RF frequency to the ion cyclotron frequency of hydrogen on the magnetic axis

Table 2. Parameter Range for Fig. 7.

type	P_{ICRF}(MW)	P_{NBI}(MW)	Hα/HeI	W_p(kJ)	$\overline{n_e}$ ($10^{19}m^{-3}$)	T_{e0}(keV)
1	0.2-0.4	0	4.2-5.3	37	0.8	0.6
2	0.4-0.5	0	3.3-4.5	34-56	0.5-0.9	0.6-1.3
3	0.3-0.4	0	1.1-1.5	24-37	0.4-0.6	0.8
4	0.9-1.4	0-2.5	0.6-6.8	40-230	0.5-1.2	1.0-3.1
5	1.0-1.3	0-3.5	0.7-4.8	180-740	1.0-6.1	1.3-2.2
6	0.5-1.0	1.4-1.6	0.6-0.8	260-320	2.1-3.0	1.7-1.9
7	1.1	1.2	0.7	160	2.2	1.3

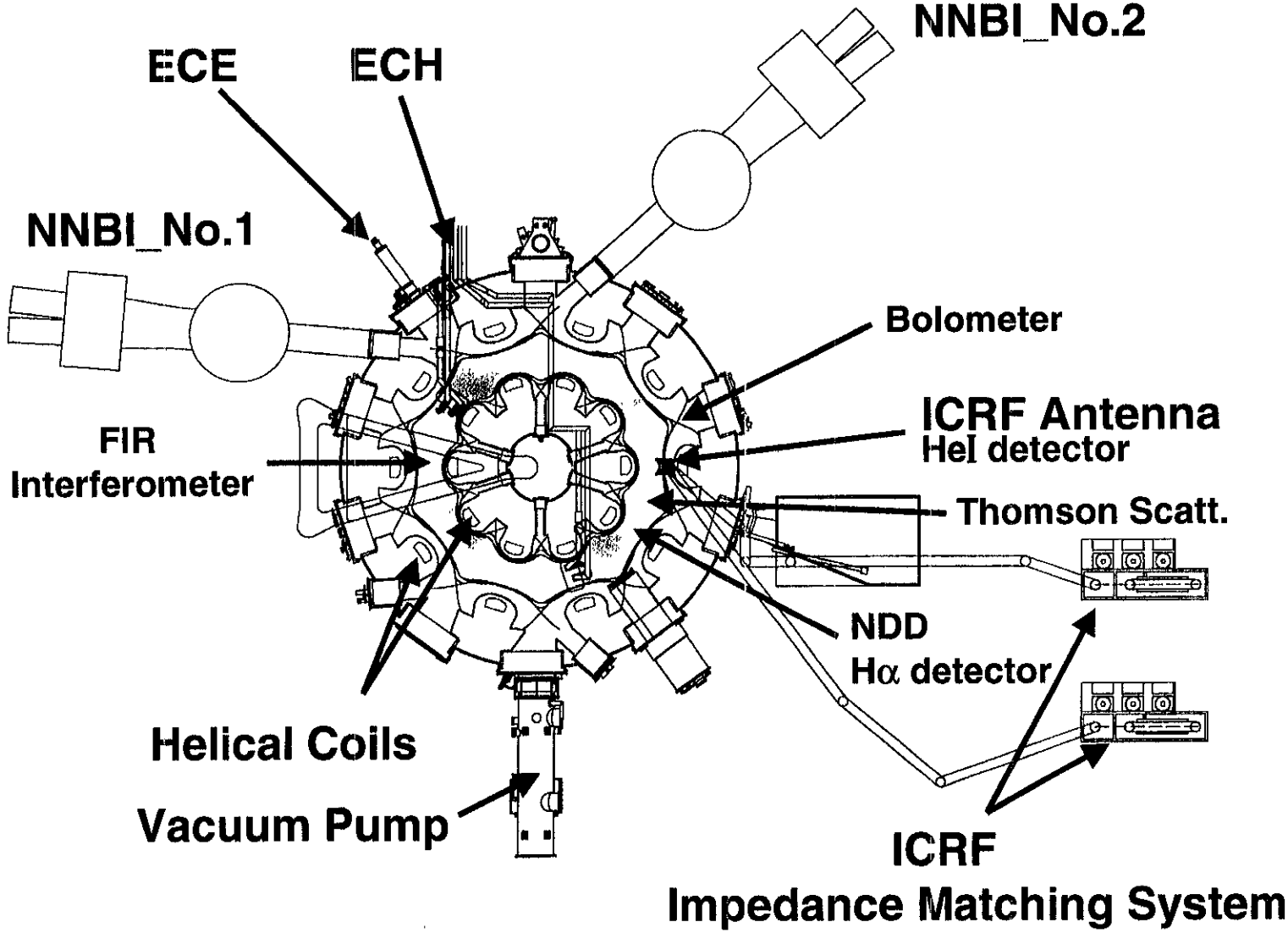
NNBI_No.2
ECE
ECH
NNBI_No.1
Bolometer
ICRF Antenna
HeI detector
FIR
Interferometer
Thomson Scatt.
NDD
Hα detector
Helical Coils
Vacuum Pump
ICRF
Impedance Matching System

Fig. 1

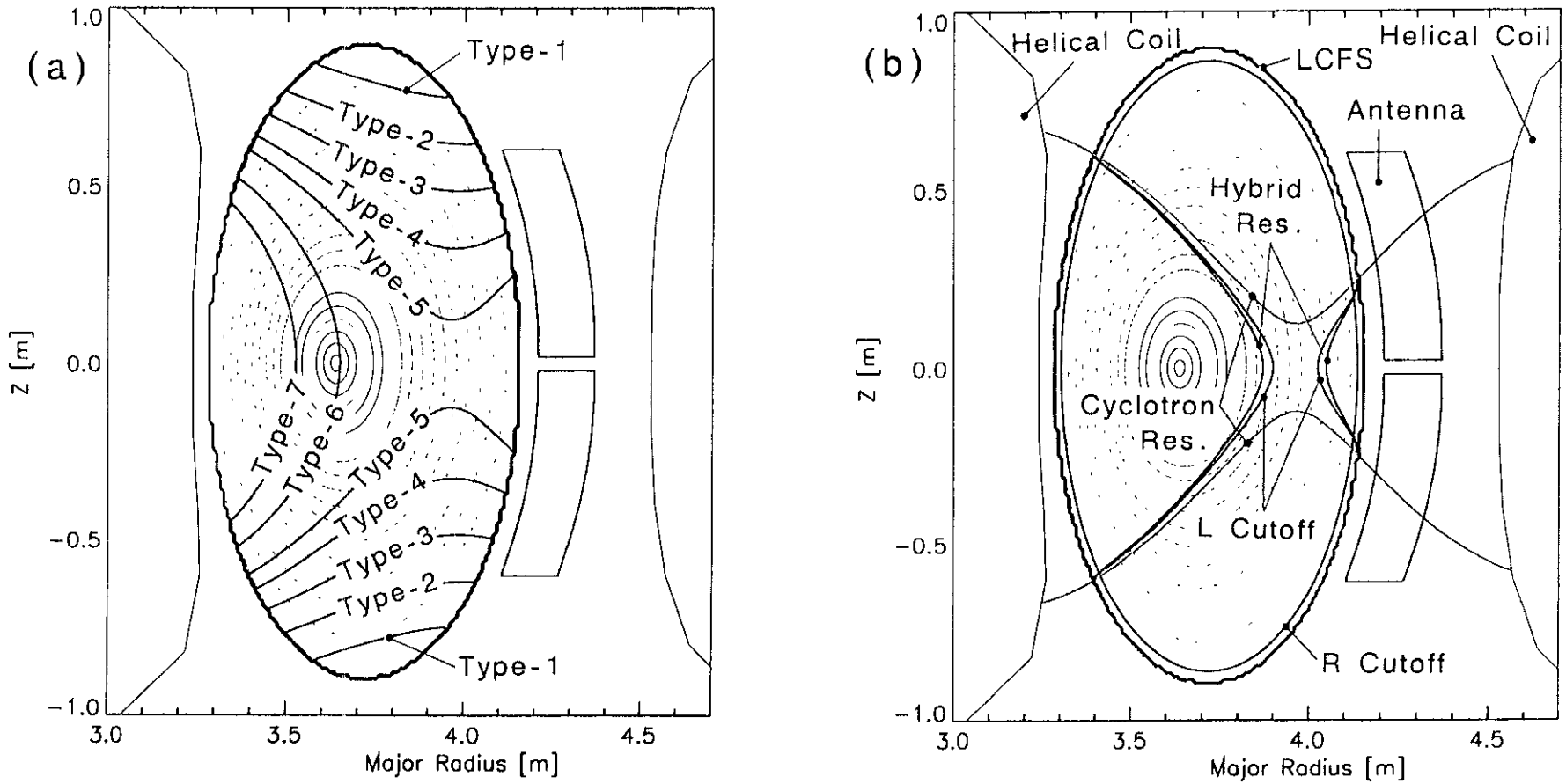
(a)
Type-1
Type-2
Type-3
Type-4
Type-5
Type-6
Type-7
Type-5
Type-4
Type-3
Type-2
Type-1
1.0
0.5
0.0
−0.5
−1.0
z [m]
3.0
3.5
4.0
4.5
Major Radius [m]
(b)
Helical Coil
LCFS
Helical Coil
Antenna
Hybrid
Res.
Cyclotron
Res.
L Cutoff
R Cutoff
1.0
0.5
0.0
−0.5
−1.0
z [m]
3.0
3.5
4.0
4.5
Major Radius [m]

Fig.2

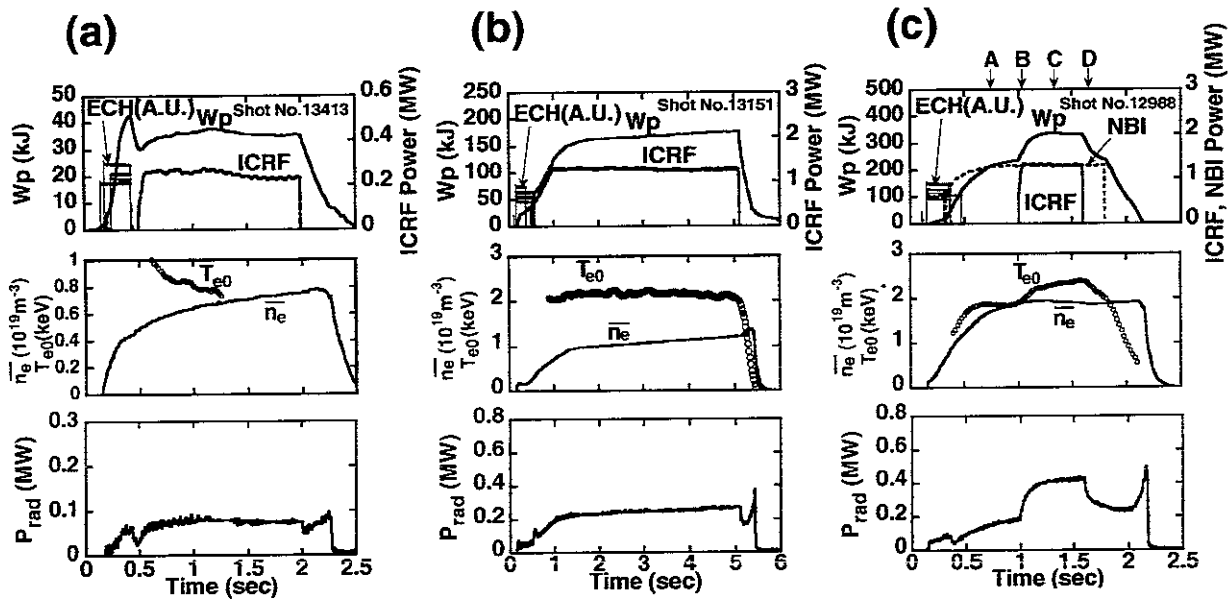
(a)
(b)
(c)
ECH(A.U.)
Wp
ICRF
NBI
Shot No.13413
Shot No.13151
Shot No.12988
A B C D
Wp (kJ)
ICRF Power (MW)
ICRF, NBI Power (MW)
T_{e0}
$\bar{n}_e$
$\bar{n}_e$ ($10^{19}m^{-3}$)
T_{e0}(keV)
P_{rad} (MW)
Time (sec)

Fig. 3

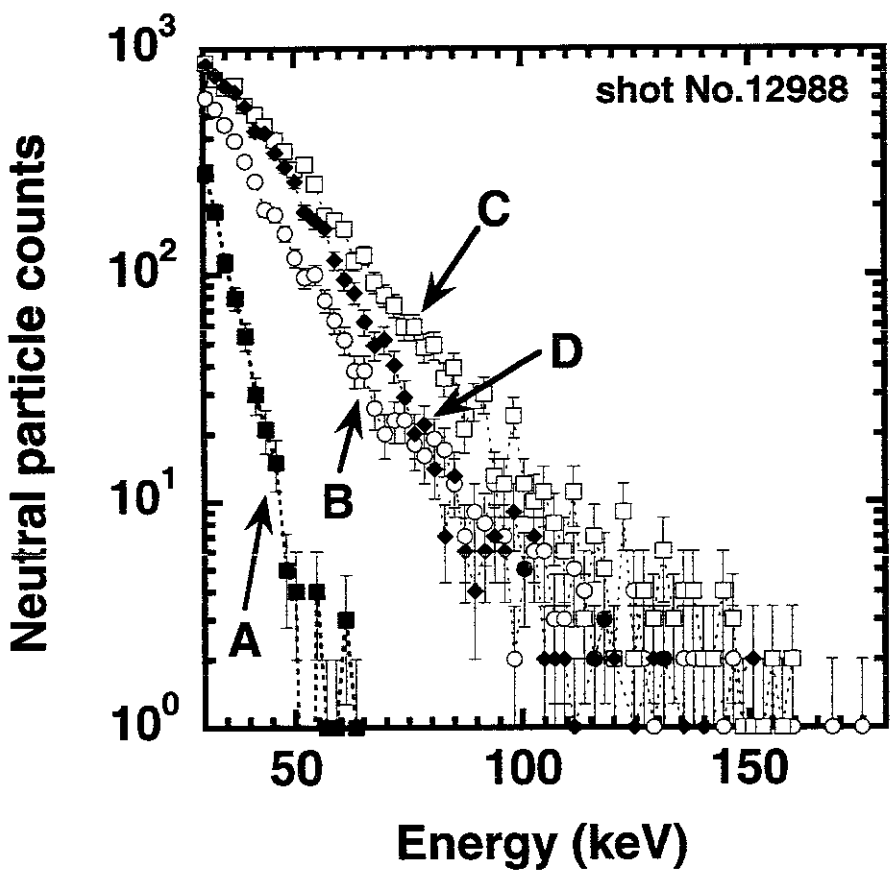
shot No.12988
A
B
C
D
Neutral particle counts
Energy (keV)
10^0
10^1
10^2
10^3
50
100
150

Fig.4

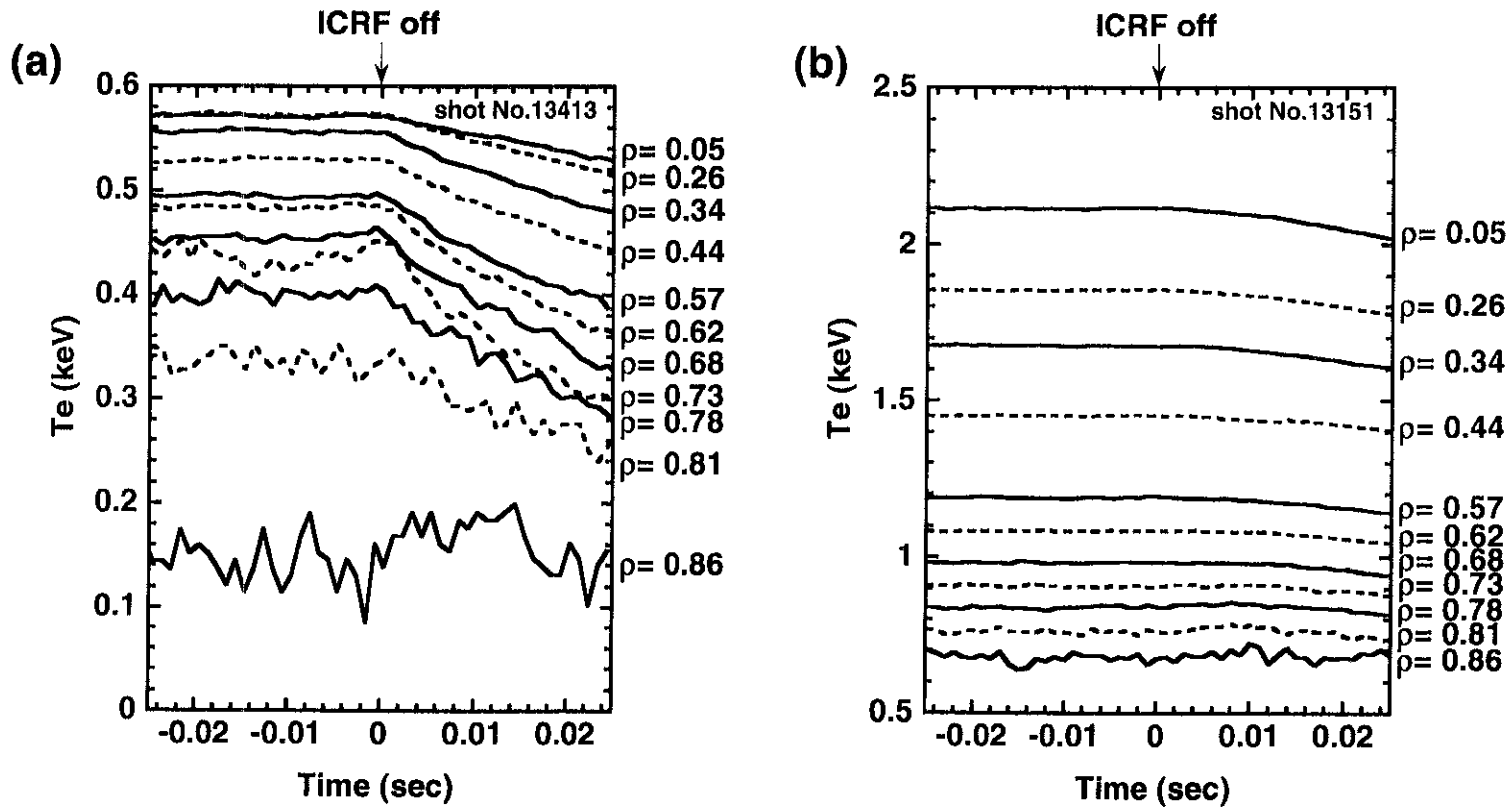
(a)
ICRF off
shot No.13413
Te (keV)
Time (sec)
ρ= 0.05
ρ= 0.26
ρ= 0.34
ρ= 0.44
ρ= 0.57
ρ= 0.62
ρ= 0.68
ρ= 0.73
ρ= 0.78
ρ= 0.81
ρ= 0.86
(b)
ICRF off
shot No.13151
Te (keV)
Time (sec)
ρ= 0.05
ρ= 0.26
ρ= 0.34
ρ= 0.44
ρ= 0.57
ρ= 0.62
ρ= 0.68
ρ= 0.73
ρ= 0.78
ρ= 0.81
ρ= 0.86

Fig. 5

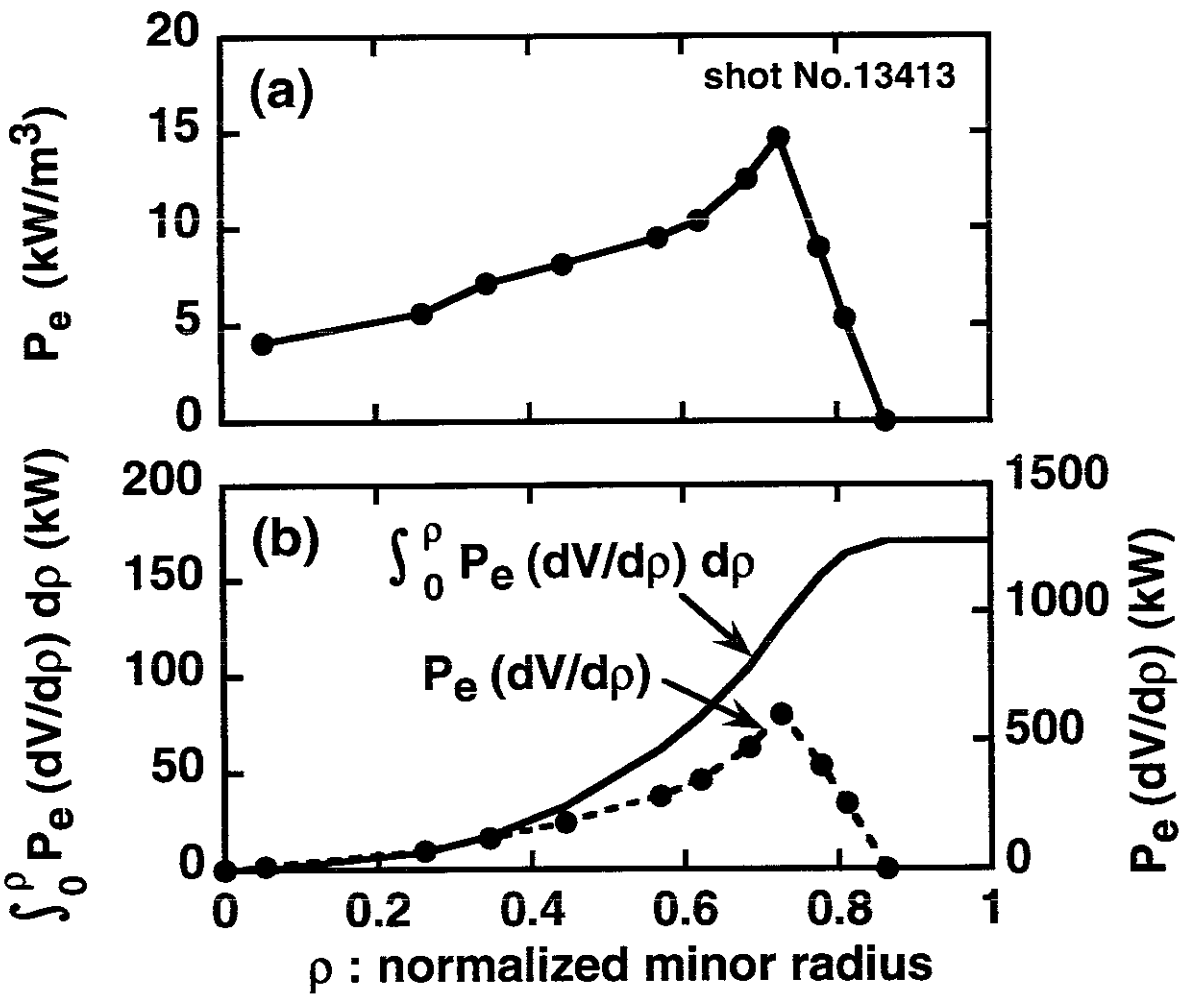
(a)
shot No.13413
P_e (kW/m^3)
20
15
10
5
0
(b)
$\int_0^\rho P_e\,(dV/d\rho)\,d\rho$
$P_e\,(dV/d\rho)$
$\int_0^\rho P_e\,(dV/d\rho)\,d\rho$ (kW)
$P_e\,(dV/d\rho)$ (kW)
200
150
100
50
0
1500
1000
500
0
0
0.2
0.4
0.6
0.8
1
ρ : normalized minor radius

Fig. 6

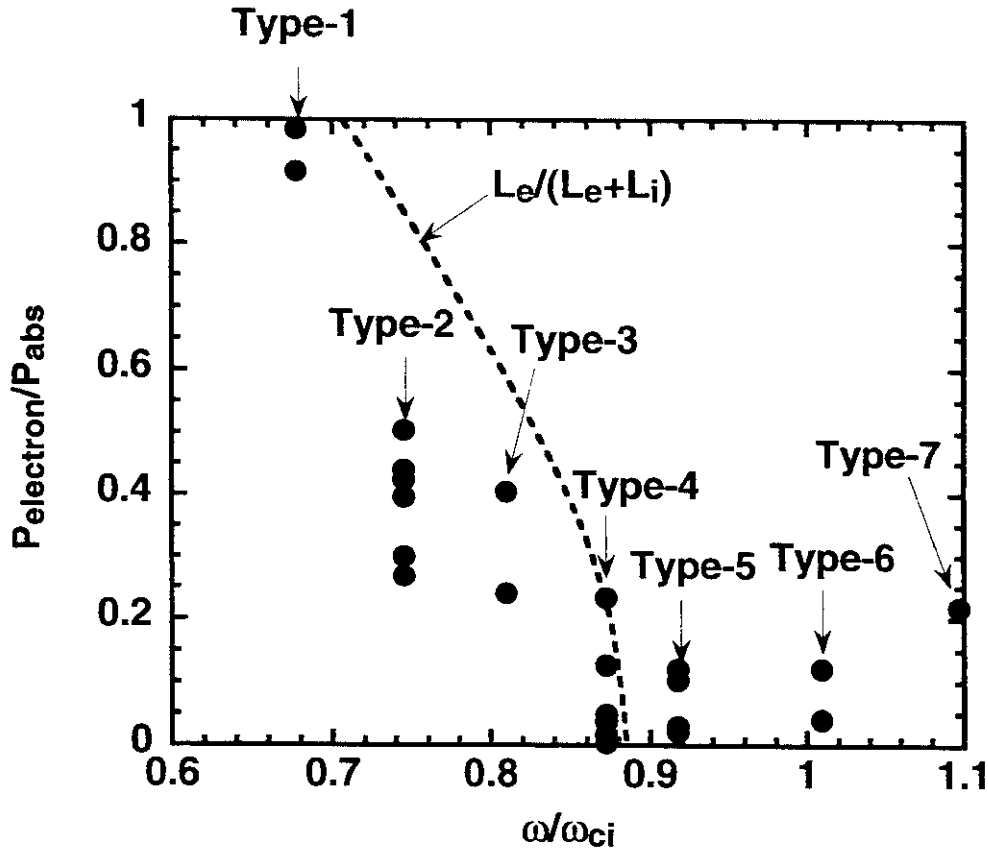
Type-1
Le/(Le+Li)
Type-2
Type-3
Type-4
Type-5
Type-6
Type-7
Pelectron/Pabs
ω/ωci
1
0.8
0.6
0.4
0.2
0
0.6
0.7
0.8
0.9
1
1.1

Fig.7

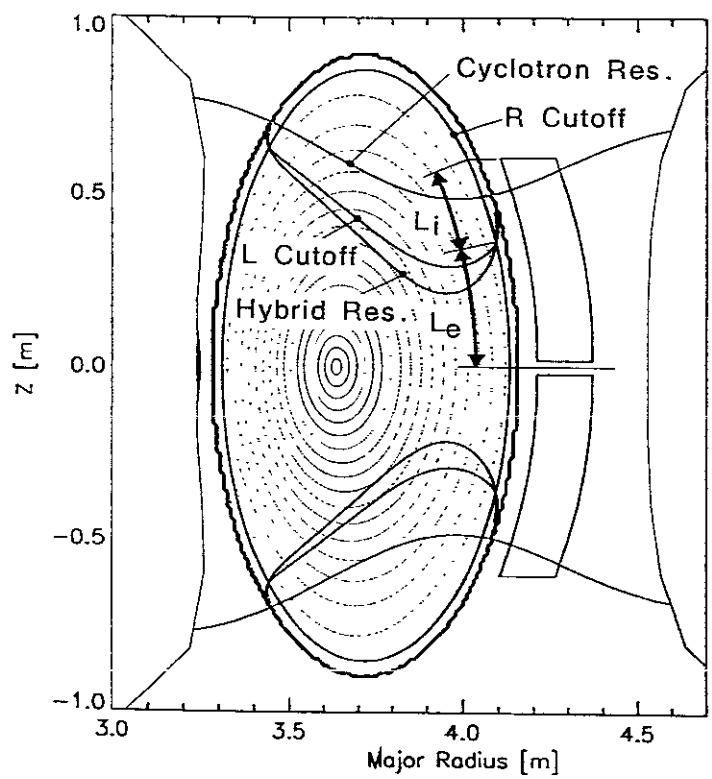
Cyclotron Res.
R Cutoff
Li
L Cutoff
Hybrid Res.
Le
z [m]
Major Radius [m]
1.0
0.5
0.0
−0.5
−1.0
3.0
3.5
4.0
4.5

Fig.8

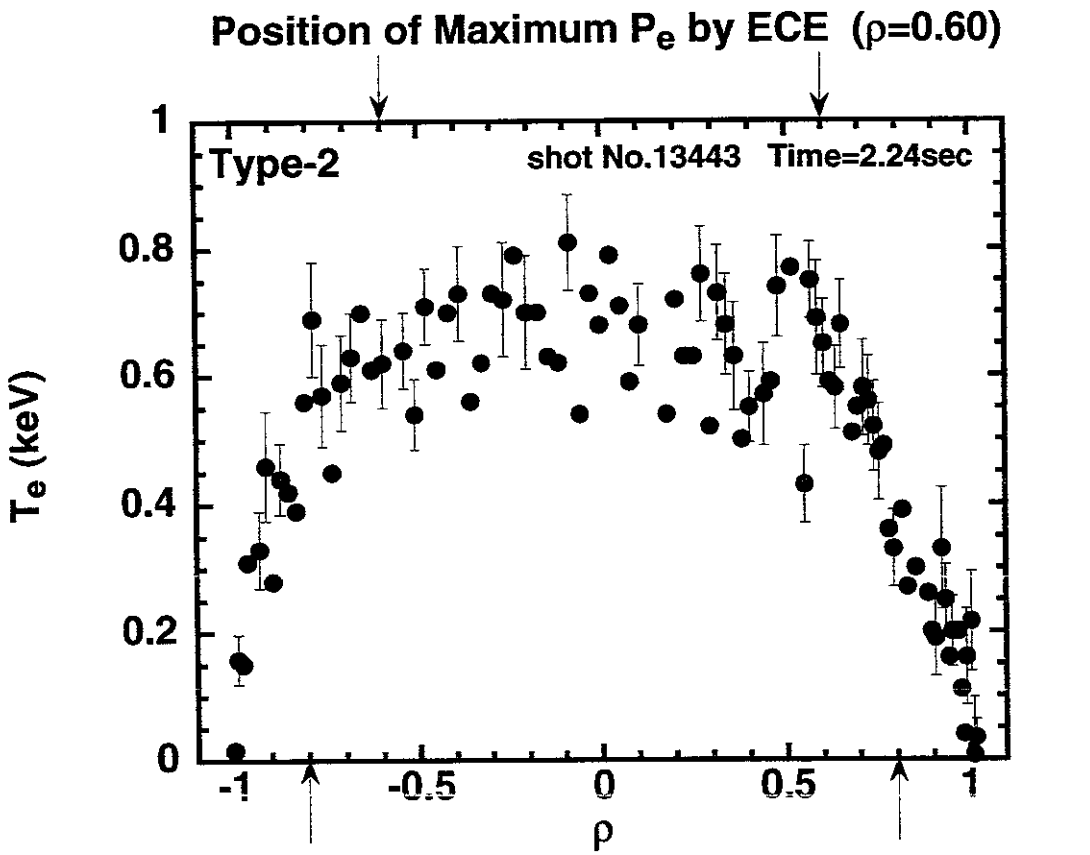
Position of Maximum P_e by ECE (ρ=0.60)
Type-2
shot No.13443 Time=2.24sec
T_e (keV)
ρ
Innermost Ion Cycrotron Resonance Layer (ρ=0.80)

Fig.9

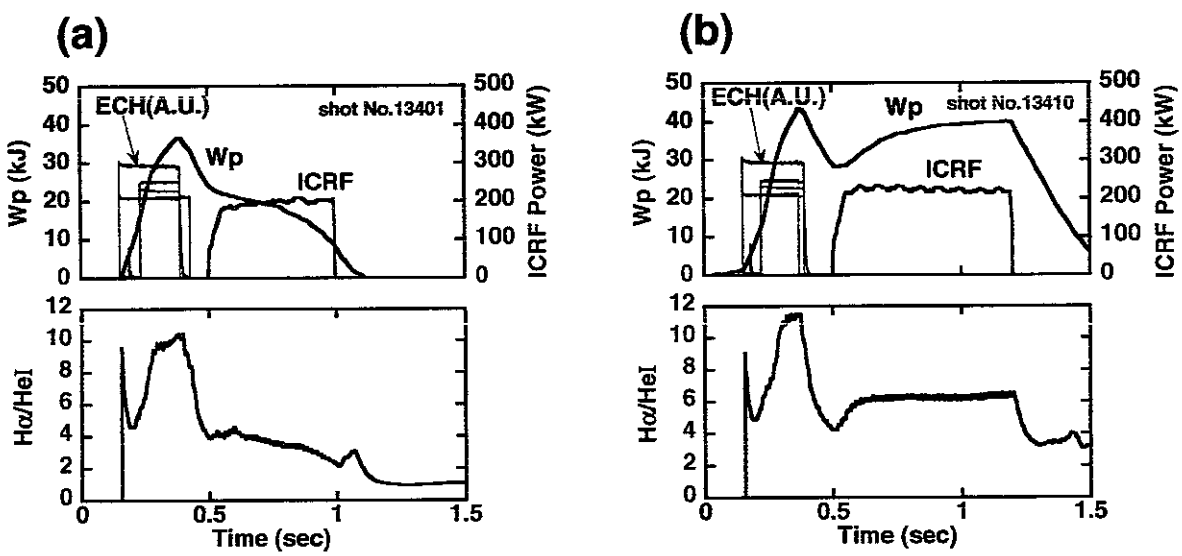
(a)
ECH(A.U.)
shot No.13401
Wp
ICRF
Wp (kJ)
ICRF Power (kW)
Hα/HeI
Time (sec)
(b)
ECH(A.U.)
Wp
shot No.13410
ICRF
Wp (kJ)
ICRF Power (kW)
Hα/HeI
Time (sec)

Fig. 10

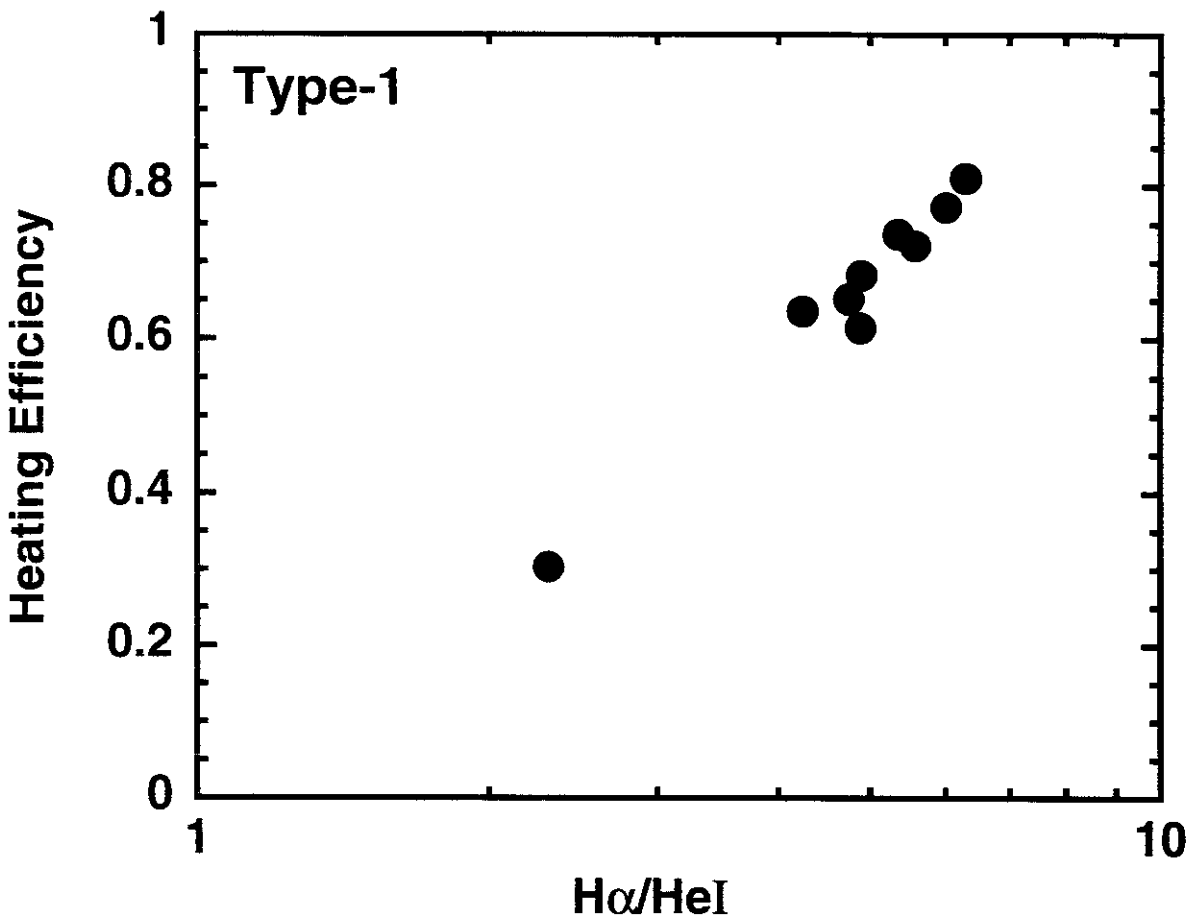

Fig.11

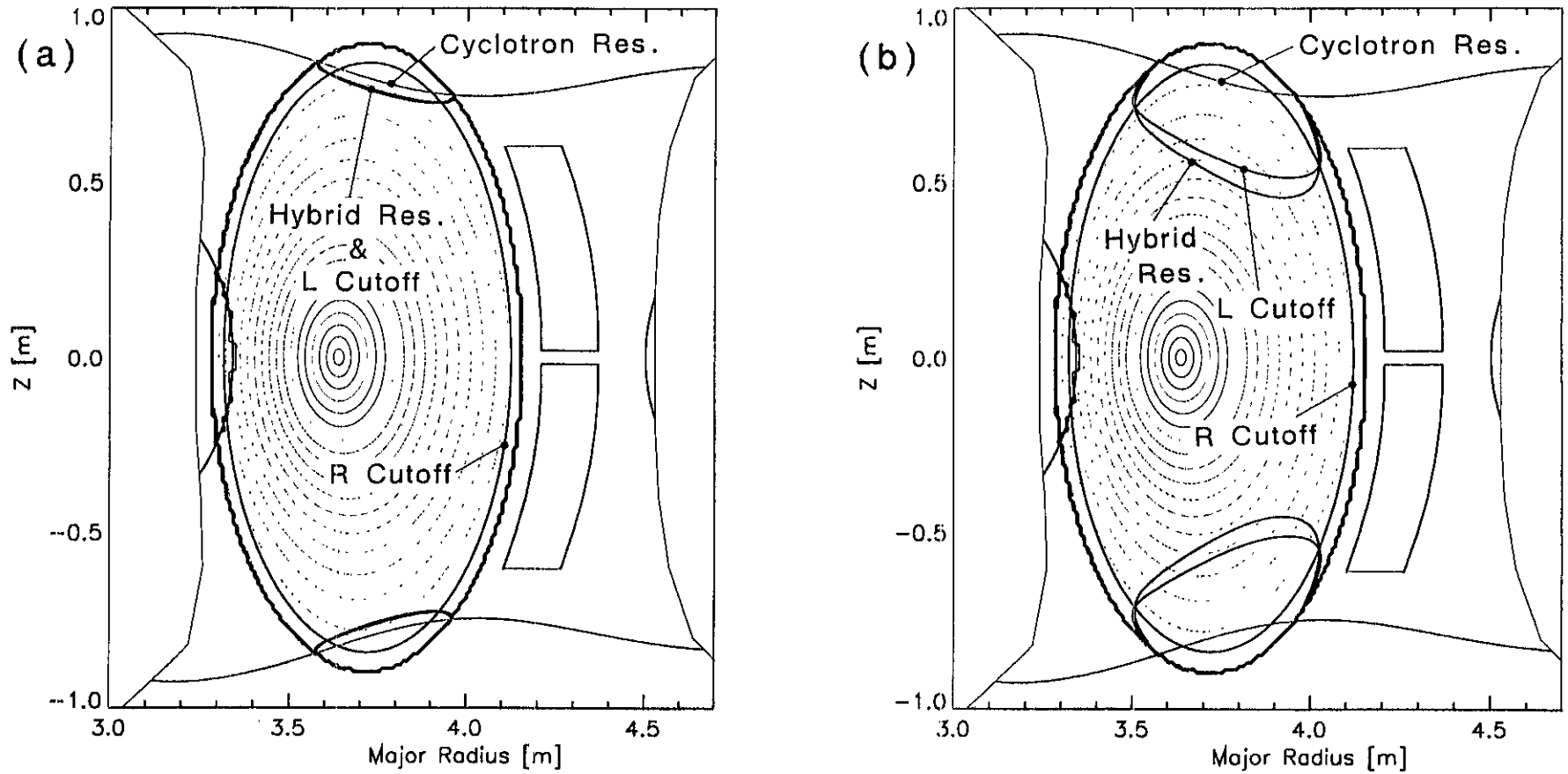
(a)
Cyclotron Res.
Hybrid Res.
&
L Cutoff
R Cutoff
1.0
0.5
0.0
−0.5
−1.0
z [m]
3.0
3.5
4.0
4.5
Major Radius [m]
(b)
Cyclotron Res.
Hybrid
Res.
L Cutoff
R Cutoff
1.0
0.5
0.0
−0.5
−1.0
z [m]
3.0
3.5
4.0
4.5
Major Radius [m]

Fig. 12

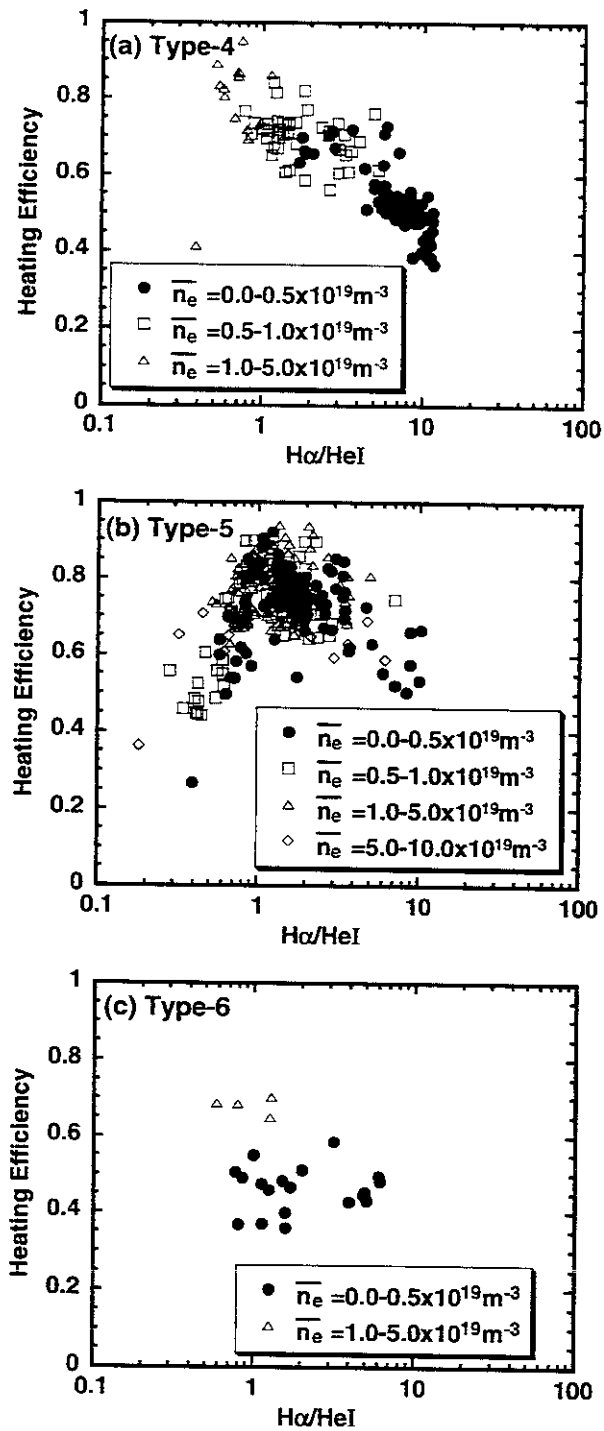
(a) Type-4
Heating Efficiency
Hα/HeI
$\overline{n_e}$ =0.0-0.5x10^{19}m^{-3}
$\overline{n_e}$ =0.5-1.0x10^{19}m^{-3}
$\overline{n_e}$ =1.0-5.0x10^{19}m^{-3}
(b) Type-5
Heating Efficiency
Hα/HeI
$\overline{n_e}$ =0.0-0.5x10^{19}m^{-3}
$\overline{n_e}$ =0.5-1.0x10^{19}m^{-3}
$\overline{n_e}$ =1.0-5.0x10^{19}m^{-3}
$\overline{n_e}$ =5.0-10.0x10^{19}m^{-3}
(c) Type-6
Heating Efficiency
Hα/HeI
$\overline{n_e}$ =0.0-0.5x10^{19}m^{-3}
$\overline{n_e}$ =1.0-5.0x10^{19}m^{-3}

Fig.13

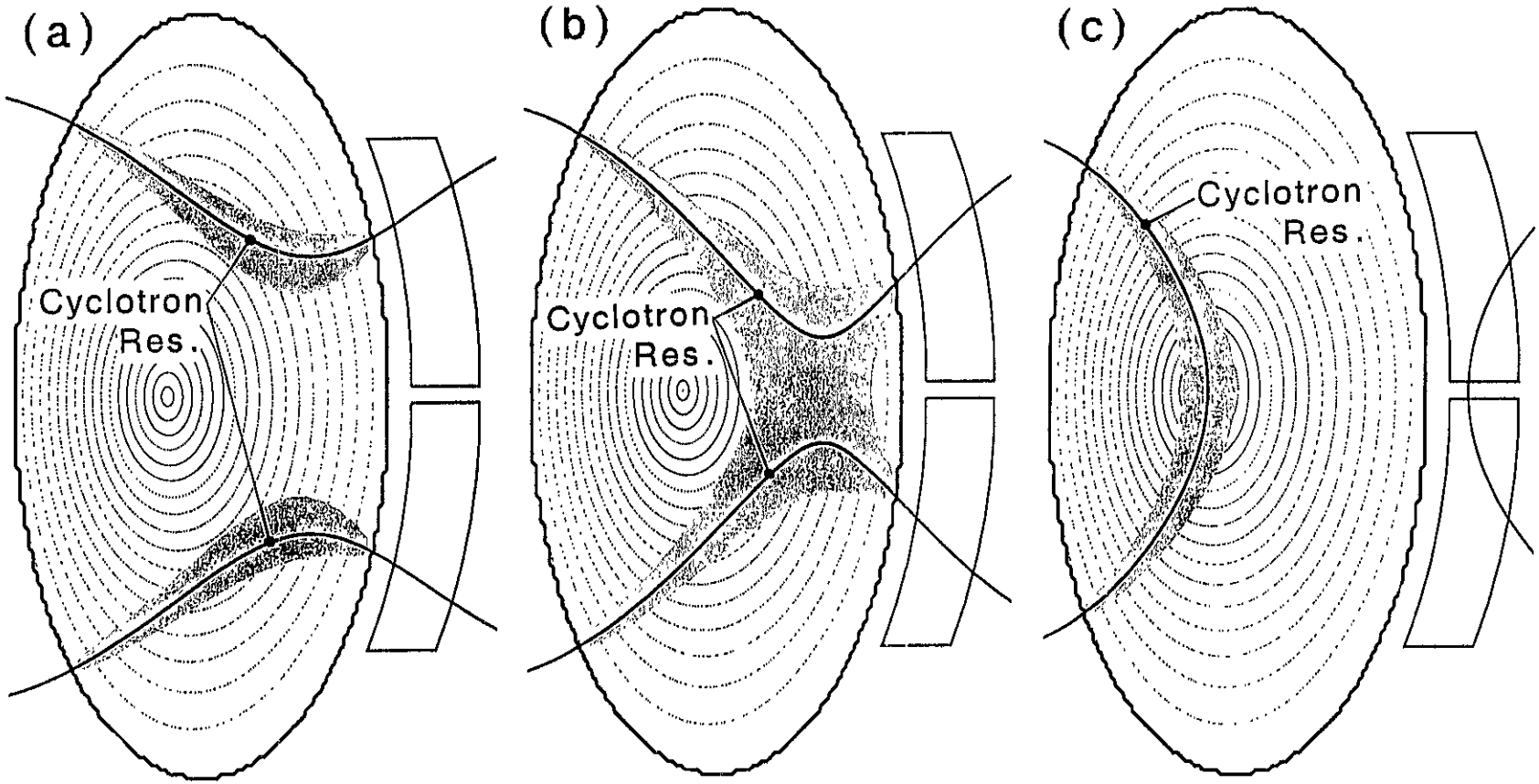

Fig. 14

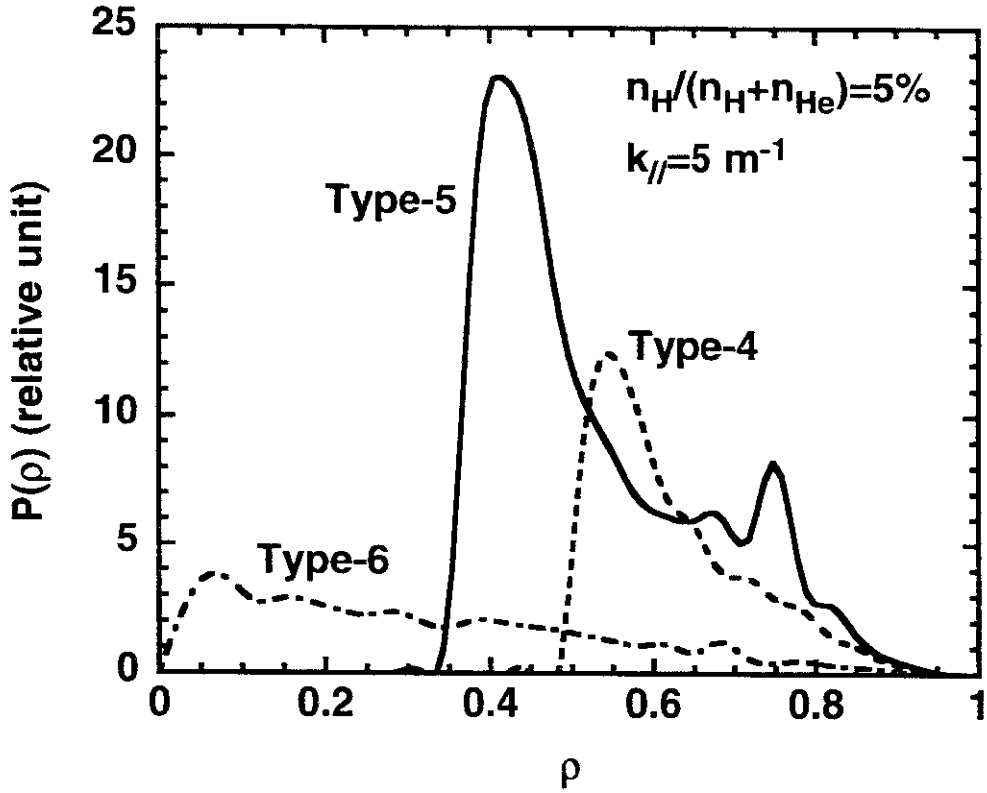
25
20
15
10
5
0
0
0.2
0.4
0.6
0.8
1
P(ρ) (relative unit)
ρ
$n_H/(n_H+n_{He})$=5%
$k_{//}$=5 m^{-1}
Type-5
Type-4
Type-6

Fig.15

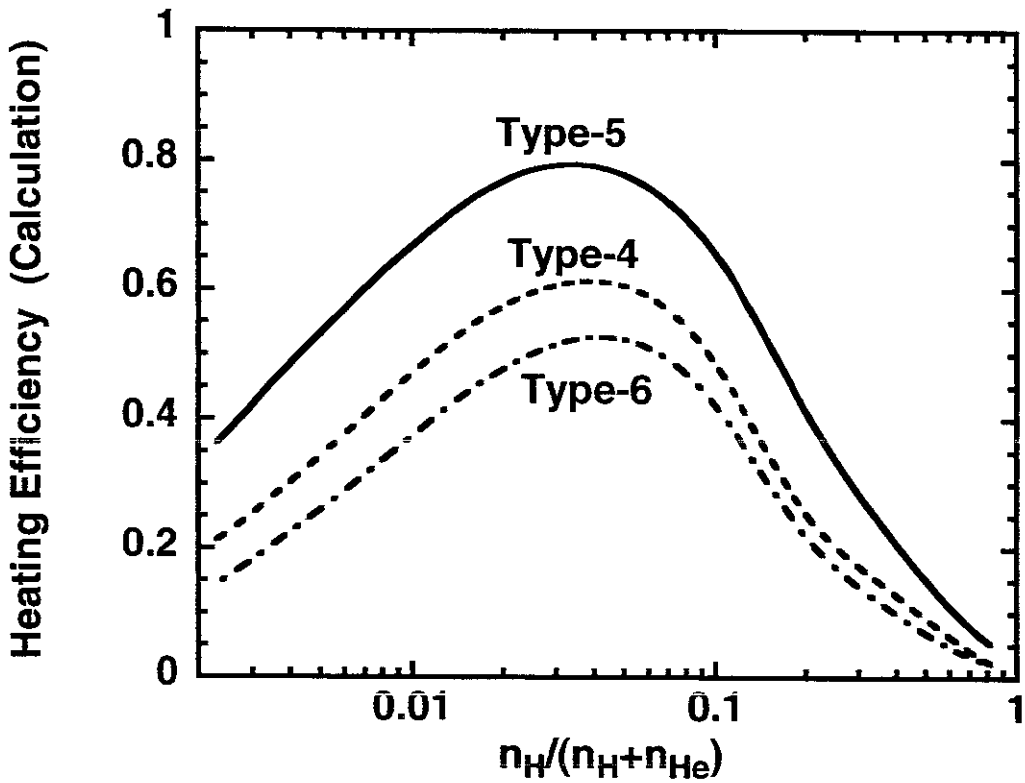
1
0.8
0.6
0.4
0.2
0
0.01
0.1
1
Heating Efficiency (Calculation)
$n_H/(n_H+n_{He})$
Type-5
Type-4
Type-6

Fig.16

Recent Issues of NIFS Series

NIFS-661 K Yamazaki, K Y Watanabe, A Sagara, H Yamada, S Sakakibara, K Narihara, K Tanaka, M Osakabe, K Nishimura, O Motojima, M Fujiwara, the LHD Group
Helical Reactor Design Studies Based on New Confinement Scalings Sep 2000
(IAEA-CN-77/ FTP 2/12)

NIFS-662 T Hayashi, N Mizuguchi, H Miura and T Sato
Dynamics of Relaxation Phenomena in Spherical Tokamak Sep 2000
(IAEA-CN-77THP2/13)

NIFS-663 H Nakamura and T Sato, H Kambe and K Sawada and T Saiki,
Design and Optimization of Tapered Structure of Near-field Fiber Probe Based on FDTD Simulation Oct 2000

NIFS-664 N Nakajima
Three Dimensional Ideal MHD Stability Analysis in L=2 Heliotron Systems Oct 2000

NIFS-665 S Fujiwara and T Sato,
Structure Formation of a Single Polymer Chain I Growth of trans Domains Nov 2000

NIFS-666 S Kida
Vortical Structure of Turbulence Nov 2000

NIFS-667 H Nakamura, S Fujiwara and T Sato
Rigidity of Orientationally Ordered Domains of Short Chain Molecules Nov 2000

NIFS-668 T Mutoh, R Kumazawa, T Seki, K Saito, Y Torii, F Shimpo, G Nomura, T Watari, D A Hartmann, M Yokota, K Akaishi, N Ashikawa, P deVries, M Emoto, H. Funaba, M Goto, K Ida, H Idei, K Ikeda, S Inagaki, N Inoue, M Isobe, O Kaneko, K Kawahata, A Komori, T Kobuchi, S Kubo, S Masuzaki, T Morisaki, S Morita, J Miyazawa, S Murakami, T Minami, S Muto, Y Nagayama, Y Nakamura, H Nakanishi, K Narihara, N Noda, K Nishimura, K Ohkubo N Ohyabu, S Ohdachi, Y Oka, M Osakabe, T Ozaki, B J Peterson, A Sagara, N Sato, S Sakakibara, R Sakamoto, H Sasao, M Sasao, M Sato, T Shimozuma, M Shoji, S Sudo H Suzuki, Y Takeiri, K Tanaka, K Toi, T Tokuzawa, K Tsumori K Y Watanabe, T Watanabe, H Yamada, I Yamada, S Yamaguchi, K Yamazaki, M Yokoyama, Y Yoshimura, Y Hamada, O Motojima, M Fujiwara,
Fast- and Slow-Wave Heating of Ion Cyclotron Range of Frequencies in the Large Helical Device Nov 2000

NIFS-669 K Mima, M S Jovanovic, Y Sentoku, Z-M Sheng, M M Skoric and T Sato,
Stimulated Photon Cascade and Condensate in Relativistic Laser-plasma Interaction Nov 2000

NIFS-670 L Hadzievski, M M Skoric and T Sato,
On Origin and Dynamics of the Discrete NLS Equation Nov 2000

NIFS-671 K Ohkubo, S Kubo, H Idei, T Shimozuma, Y Yoshimura, F Leuterer, M Sato and Y Takita,
Analysis of Oversized Sliding Waveguide by Mode Matching and Multi-Mode Network Theory Dec 2000

NIFS-672 C Das, S Kida and S Goto,
Overall Self-Similar Decay of Two-Dimensional Turbulence Dec 2000

NIFS-673 L A Bureyeva, T Kato, V S Lisitsa and C Namba,
Quasiclassical Representation of Autoionization Decay Rates in Parabolic Coordinates Dec 2000

NIFS-674 L A Bureyeva, V S Lisitsa and C Namba,
Radiative Cascade Due to Dielectronic Recombination Dec 2000

NIFS-675 M FHeyn, S V Kasilov, W Kernbichler, K Matsuoka, V V Nemov, S Okamura, O S. Pavlichenko,
Configurational Effects on Low Collision Plasma Confinement in CHS Heliotron/Torsatron, Jan 2001

NIFS-676 K Itoh,
A Prospect at 11th International Toki Conference - Plasma physics, quo vadis?, Jan 2001

NIFS-677 S Satake, H Sugama, M Okamoto and M Wakatani,
Classification of Particle Orbits near the Magnetic Axis in a Tokamak by Using Constants of Motion, Jan 2001

NIFS-678 M Tanaka and A Yu Grosberg,
Giant Charge Inversion of a Macroion Due to Multivalent Counterions and Monovalent Coions Molecular Dynamics Studyn, Jan 2001

NIFS-679 K Akaishi, M Nakasuga, H Suzuki, M Iima, N Suzuki, A Komori O. Motojima and Vacuum Engineering Group
Simulation by a Diffusion Model for the Variation of Hydrogen Pressure with Time between Hydrogen Discharge Shots in LHD, Feb 2001

NIFS-680 A Yoshizawa, N Yokoi, S Nisizima, S -I Itoh and K. Itoh
Variational Approach to a Turbulent Swirling Pipe Flow with the Aid of Helicity, Feb 2001

NIFS-681 Alexander.A.Shishkin
Estafette of Drift Resonances, Stochasticity and Control of Particle Motion in a Toroidal Magnetic Trap, Feb 2001

NIFS-682 H Momota and G H Miley,
Virtual Cathode in a Spherical Inertial Electrostatic Confinement Device Feb 2001

NIFS-683 K Saito, R Kumazawa, T Mutoh, T Seki, T Watari, Y Torii, D A Hartmann, Y Zhao, A Fukuyama, F Shimpo, G Nomura, M Yokota, M Sasao, M Isobe, M Osakabe, T Ozaki, K Narihara, Y Nagayama, S Inagaki, K Itoh, S Morita, A V Krasilnikov, K Ohkubo, M Sato, S Kubo, T Shimozuma, H Idei, Y Yoshimura, O Kaneko, Y Takeiri, Y Oka, K Tsumori, K Ikeda, A Komori, H Yamada, H Funaba, K Y Watanabe, S Sakakibara, M. Shoji, R Sakamoto, J Miyazawa, K Tanaka, B J Peterson, N Ashikawa, S Murakami, T Minami, S. Ohdachi, S Yamamoto, S Kado, H Sasao, H Suzuki, K Kawahata, P deVries, M Emoto, H Nakanishi, T Kobuchi, N Inoue, N Ohyabu, Y Nakamura, S Masuzaki, S Muto, K Sato, T Morisaki, M Yokoyama, T Watanabe, M Goto, I Yamada, K Ida, T Tokuzawa, N Noda, S Yamaguchi, K Akaishi, A Sagara, K Toi, K Nishimura, K Yamazaki, S Sudo, Y Hamada, O Motojima, M Fujiwara,
Ion and Electron Heating in ICRF Heating Experiments on LHD Mar 2001